Joule

CellPress

Article

Interplay of Lithium Intercalation and Plating on a Single Graphite Particle

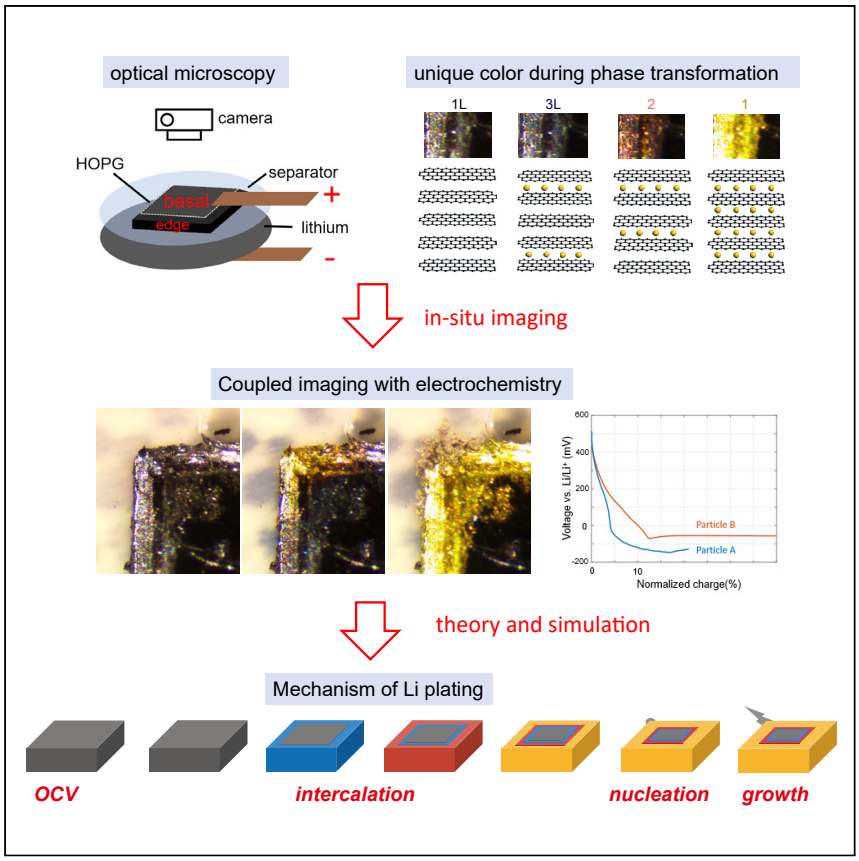

Lithium plating in graphite electrodes is a side reaction that prevents the fast charging of Li-ion batteries. Understanding its mechanism and onset condition is critical for effective material design, cell engineering, and battery management to realize fast charging. This work revealed the lithium plating mechanism on single graphite particles by combining *in situ* experiments with theory and simulation.

Tao Gao, Yu Han, Dimitrios Fraggedakis, ..., William C. Chueh, Ju Li, Martin Z. Bazant

bazant@mit.edu

HIGHLIGHTS

Visualized the phase transformation of graphite particles and lithium plating on them

Revealed the mechanism of lithium plating on graphite and its onset condition

Elucidated the interplay between lithium insertion and plating in the graphite electrode

Developed a theory to model the onset of lithium plating

Gao et al., Joule 5, 1–22
February 17, 2021
https://doi.org/10.1016/j.joule.2020.12.020

Please cite this article in press as: Gao et al., Interplay of Lithium Intercalation and Plating on a Single Graphite Particle, Joule (2021), https://doi.org/10.1016/j.joule.2020.12.020

Joule

CellPress

Article

Interplay of Lithium Intercalation and Plating on a Single Graphite Particle

Tao Gao,[1,9] Yu Han,[1] Dimitrios Fraggedakis,[1] Supratim Das,[1] Tingtao Zhou,[2] Che-Ning Yeh,[3] Shengming Xu,[4] William C. Chueh,[3] Ju Li,[5,6] and Martin Z. Bazant[7,8,10,*]

SUMMARY

Improving safety while increasing the charging rates and extending the lifetime is the grand challenge for lithium-ion batteries. The key challenge is to control lithium plating, a parasitic reaction on graphite anodes that competes with lithium intercalation. Here, we determine the fundamental mechanism for the onset of lithium plating on graphite particles. We perform *in situ* optical microscopy coupled with electrochemical measurements to resolve the spatial dynamics of lithiation and plating on the surface of a single graphite particle. We observe that the onset of plating is strongly coupled with phase separation in graphite and occurs only on the fully lithiated edges of the particles. The competition between Li insertion and plating is further elucidated by examining the energetics and kinetics of both reactions. Based on the physical insights drawn from the experiments, we propose a phase-field model that predicts the onset of Li plating.

INTRODUCTION

The electrification of transportation is a promising means to reduce the dependence of our societies on fossil fuels. Lithium-ion batteries (LIBs) have become the dominant technology to power electric vehicles (EVs), but there are still many issues hindering their widespread adoption. One major challenge is the risk of thermal runaway, which can cause safety accidents.[1] Another challenge is the long time required to recharge a LIB (at least 40 min for 80% of the total battery capacity).[2] Extreme fast charging (80% capacity within 10 min) still remains elusive due to rapid capacity fading and potential safety hazards.[3] Overcoming both challenges has been linked to controlling the onset of lithium (Li) metal plating, a detrimental side reaction that may occur on graphite anodes during battery operation.[4]

During battery charging, Li ions are extracted from the cathode and transported through the electrolyte toward the anode, where they are reduced (Figure 1A). The desired reaction is Li-ion insertion (or intercalation) into the layered structure of graphite, but Li ions can also be directly reduced to metallic Li under certain conditions, such as high charging rates or low temperatures.[5] Even trace amounts of Li plating can affect the performance, durability, and operational safety of LIBs in several ways: (1) capacity fading occurs due to loss of Li inventory, which results from the deactivation of the plated Li or formation of solid electrolyte interphases (SEI) on the formed Li metal[6–9]; (2) internal resistance can increase due to pore clogging by plated Li, which hinders ion transport in the porous electrode[10,11]; and (3) there is an increasing risk of short circuit, and thus thermal runway, due to the formation of Li metal dendrites.[1,12] In order to address these problems, it is critical to

Context & Scale

The long charging time (40 min or longer) of electric vehicles compared with the short refueling time of gasoline cars (several minutes) is one of the main barriers preventing the wide adoption of EVs. Under fast charging conditions, side reactions happen inside a lithium-ion battery, significantly compromising its performance and safety. Addressing this challenge first requires an in-depth understanding of the mechanism of these side reactions. This work focuses on lithium plating on graphite particle, the most important side reaction that governs battery's safety and cycle life. By combining *in situ* experiment with theory and simulation, we successfully elucidated the mechanism and onset condition of lithium plating on graphite particles, which provides fundamental insights for material design, cell engineering, and battery management to achieve fast charging.

Please cite this article in press as: Gao et al., Interplay of Lithium Intercalation and Plating on a Single Graphite Particle, Joule (2021), https://doi.org/10.1016/j.joule.2020.12.020

establish a quantitative understanding of the Li plating mechanism on graphite to guide material design and battery engineering. Particularly, these questions need to be answered: (1) when Li plating happens in a Li-ion battery? (2) where it happens in the graphite anode?; (3) how it initiates, grows, and causes internal short circuit?; and (4) to what extent can the deposited Li be re-utilized? Among them, the timing of Li plating is especially important because it marks the onset of Li plating and determines the safe operation window of a Li-ion battery.

There exist different hypotheses to determine the onset of Li plating(Table 1; Figures 1B–1D). The most common one is based on equilibrium thermodynamics.[3,4,13] By definition, the plating reaction becomes thermodynamically possible when the voltage of graphite drops below 0 V versus Li/Li^+ (Figure 1B).[14,15] This can occur if the intercalation reaction is kinetically difficult, and the resulted large overpotential can exceed the equilibrium voltage of the last phase transformation in Li-graphite phase diagram and bring the voltage of graphite below 0 V Li/Li^+. Although this voltage criterion is a necessary condition for Li plating to occur, it is not sufficient as demonstrated in many experiments. For example, experiments have shown that graphite anodes can tolerate large negative voltages (−200 to − 400 mV) before any Li plating is observed,[15–18] in which case the onset of plating occurs far from equilibrium.

To account for such non-equilibrium phenomena, the dynamics of the system needs to be considered. Especially, mass transport limitation is known to be an important factor. Since intercalation consumes Li/Li^+ from the electrolyte,[21] the salt concentration near the graphite surface can become depleted ($c_l \rightarrow 0$) (Figure 1C), whenever the applied current is large compared to the salt diffusion in the electrolyte. The large concentration polarization can drop the potential below 0 V,[22] and the complete depletion of ions can trigger metal deposition in the form of dendrite growth, in which tip splitting growth moves the interface forward to chase the concentration profile.[23] This mechanism is termed as diffusion-limited aggregation, which explains the dendrite deposition of zinc,[24] copper,[25] and recently has been confirmed to cause dendritic lithium formation on Li metal substrate under high charging rate.[19] However, it is not clear whether the same scenario applies to graphite. Another possible mechanism is the solid diffusion limitation in graphite.[20] Since Li occupies interstitial sites in the graphite lattice, the surface can become saturated by the inserted ions if solid diffusion is slow compared to intercalation ($c \rightarrow 1$) (Figure 1D).[26,27] As a result of surface crowding,[28,29] the intercalation rate is drastically reduced, and the applied current can be redirected to the formation of Li metal, leading to Li plating. Indeed, Li metal has been observed to grow preferentially on fully lithiated graphite particles in "unrolled" porous electrodes,[30] albeit without resolving either solid or liquid concentration gradients.

In efforts to identify the mechanism of Li plating on graphite, experiments and modelings have been focusing on porous electrodes. Li plating on a graphite electrode is highly heterogeneous and localized to a certain region.[31,32] Reaction heterogeneity among graphite particles, observed in both the depth direction[30,33] and lateral direction[34] of the porous electrodes, are believed to correlate to the localized Li plating. In depth direction, Li plating typically occurs on the separator side,[30,33] which was attributed to electrolyte transport limitations.[35,36] However, the origin of the lateral heterogeneity of Li plating is still not clear.[37] These electrode-scale studies provide a global view on Li plating events in graphite electrode; however, how Li plating competes with graphite filling in the local environment is not clear. We are not aware of any direct observation of Li plating during phase separation

[1]Department of Chemical Engineering, Massachusetts Institute of Technology, Cambridge, MA 02139, USA

[2]Department of Physics, Massachusetts Institute of Technology, Cambridge, MA 02139, USA

[3]Department of Material Science and Engineering, Stanford University, Stanford, CA 94305, USA

[4]Institute of Nuclear and New Energy Technology, Tsinghua University, Beijing 100084, China

[5]Department of Nuclear Science and Engineering, Massachusetts Institute of Technology, Cambridge, MA 02139, USA

[6]Department of Material Science and Engineering, Massachusetts Institute of Technology, Cambridge, MA 02139, USA

[7]Department of Chemical Engineering, Massachusetts Institute of Technology, Cambridge, MA 02139, USA

[8]Department of Mathematics, Massachusetts Institute of Technology, Cambridge, MA 02139, USA

[9]Present address: Department of Chemical Engineering, the University of Utah, UT 84112, USA

[10]Lead Contact

*Correspondence: bazant@mit.edu

https://doi.org/10.1016/j.joule.2020.12.020

Please cite this article in press as: Gao et al., Interplay of Lithium Intercalation and Plating on a Single Graphite Particle, Joule (2021), https://doi.org/10.1016/j.joule.2020.12.020

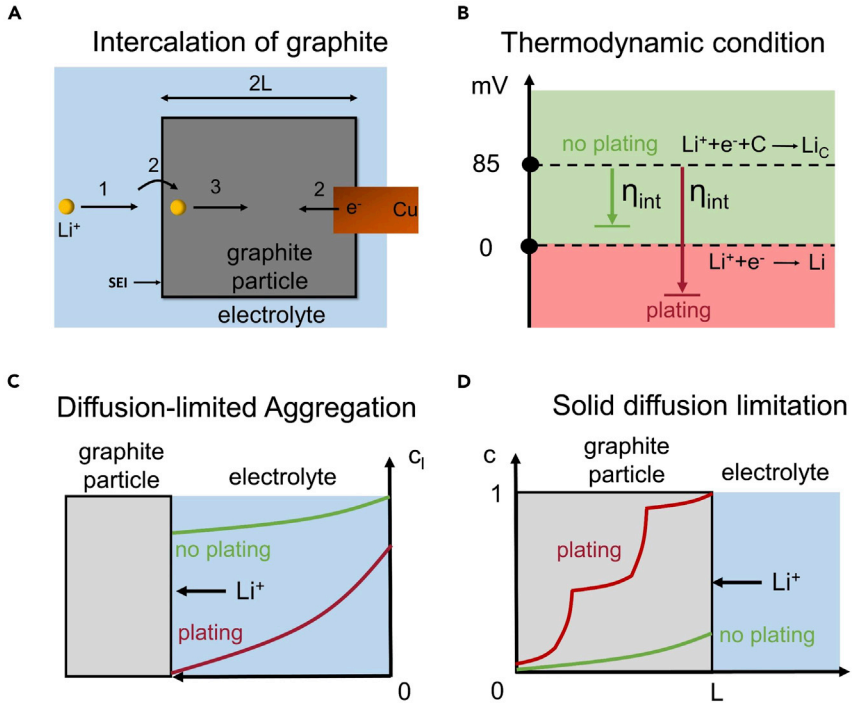

Figure 1. Proposed Mechanisms of Li Plating on Graphite

(A) 2D schematic of intercalation of a graphite particle. Three sequential steps take place during charging at the graphite anode: (1) Li^+ transport in electrolyte toward the reaction site; (2) Li^+ intercalation into a graphite particle (including de-solvation and migration through SEI); and (3) Li^+ solid diffusion within the graphite particle.

(B) Thermodynamic criterion for Li plating (V<0 versus Li/Li^+). The green and red arrows illustrate the required overpotentials to drive the insertion reaction at small current/fast insertion kinetics and large current/slow insertion kinetics. The thermodynamic criterion can be satisfied when the overpotential η_{int} is larger than the equilibrium voltage of the stage 2 to stage 1 phase transition (85 mV).

(C) 1D schematic of diffusion-limited aggregation resulted from electrolyte transport limitation. The green and red curves illustrate the Li^+ salt concentration profile in the electrolyte. Li plating could be triggered upon local salt depletion in the electrolyte ($c_l \rightarrow 0$), if liquid diffusion is slow compared to intercalation.

(D) 1D schematic of solid diffusion-limitation mechanism. The green and red curves illustrate the Li^+ concentration profile in the graphite particle. Li plating could occur when intercalated Li^+ saturate the graphite surface and block further insertion ($c \rightarrow 1$), if their diffusion is slow compared to intercalation.

in single graphite particles, which is necessary to elucidate the competition between plating and insertion locally. In addition to these fundamental studies, there is an emerging trend to integrate Li metal into graphite or other carbon materials to construct hybrid anodes to enhance the anode capacity.[38,39] Understanding how plated Li interacts with graphite will benefit the design of such hybrid anodes.

Mathematical models have also been developed to predict the onset of Li plating and metal growth,[14,40] but they have yet to incorporate all the relevant physics. In most cases, Li intercalation[27,41–43] and Li plating[14,44] are described through empirical Butler-Volmer kinetics, in contrast to the emerging quantum description of intercalation based on coupled ion-electron transfer theory,[45,46] which unifies Marcus theory with non-ideal thermodynamics.[28,43] Moreover, the solid-state diffusion of intercalated Li ions is usually described by Fick's Law with concentration-dependent

Please cite this article in press as: Gao et al., Interplay of Lithium Intercalation and Plating on a Single Graphite Particle, Joule (2021), https://doi.org/10.1016/j.joule.2020.12.020

Table 1. Hypothetical Li Plating Mechanisms in Graphite Anode

Hypothesis	Key Parameter	Onset Condition	Reference
Thermodynamic criterion	voltage of graphite versus Li/Li^+	$V_{graphite} < 0$	Arora et al.[14]
Diffusion-limited aggregation	Li concentration in electrolyte (c_l)	$c_l = 0$ at graphite surface	Bai et al.[19]
Solid diffusion limitation	Li concentration in graphite (c)	$c = 1$ at graphite surface	Legrand et al.[20]

diffusivities,[20,30] neglecting staging phase separation, and more realistic phase-field models of graphite[26,27,42,43] have not yet included a model of Li plating, due to the absence of experimental guidance.

In this work, we aim to systematically describe the fundamental mechanism of the onset of Li plating on graphite particles by combining experiments with physics-based modeling. Although graphite surface chemistry plays a key role in regulating the plating behavior,[47,48] the emphasis of this work is to illuminate the physics of phase transformation and reactions of graphite particles and examine the proposed Li plating mechanisms (Figure 1). To achieve this goal, we first use *in-operando* optical microscopy complemented by electrochemical measurements to concurrently monitor the Li concentration and the voltage of graphite single particles during battery cycling. Optical microscopy exploits the unique colors of different graphite phases[30,34] and allows us to track the coupled dynamics of Li intercalation, phase separation, and Li plating without the complexity of population dynamics at the electrode scale.[34,42,43] Based on our observations, we develop a simple physical picture to elucidate the interplay of Li insertion and plating on graphite particles and further build a phase-field model to predict the onset of Li plating. The fundamental insights gained in this study and the mathematical model can be used to guide the design of advanced materials and electrodes, as well as charging algorithms to achieve extreme fast charging.

RESULTS

Experiments

We choose highly oriented pyrolytic graphite (HOPG) as the model system for the study. HOPG is a highly pure and ordered form of synthetic graphite. It is polycrystalline with a very low mosaic spread angle, i.e., the individual graphite crystals are well aligned with each other. We designed a custom electrochemical cell for *operando* optical imaging of single HOPG particles (1 mm × 1 mm × 0.1–0.2 mm) during battery cycling (Figure 2). The lithiation and de-lithiation of the HOPG particle was done via a HOPG/electrolyte/Li sandwich. The basal plane and part of the edge plane is visualized and recorded during the experiment using a stereomicroscope and digital camera. We note this work is a fundamental study, and we do not intend to show any performance. Although the graphite particle size (1 mm) is larger than the practical particle sizes, the underlying physics of competing reactions at graphite surfaces and phase changes are the same.

Since the different phases of Li-graphite intercalation compounds have different colors (Figures 2C and 2D), the concentration of Li in the graphite particle in these stages can be inferred from the color. In order to observe the edge surface, the sides of the graphite particles were intentionally treated to expose part of the edge surface. A typical lithiation voltage curve of micron-sized graphite at quasi-equilibrium condition is shown in Figure 2C. Different phases are marked by their corresponding colors.[30,34,49] Phase transformation is characterized by a plateau in the voltage curve

Please cite this article in press as: Gao et al., Interplay of Lithium Intercalation and Plating on a Single Graphite Particle, Joule (2021), https://doi.org/10.1016/j.joule.2020.12.020

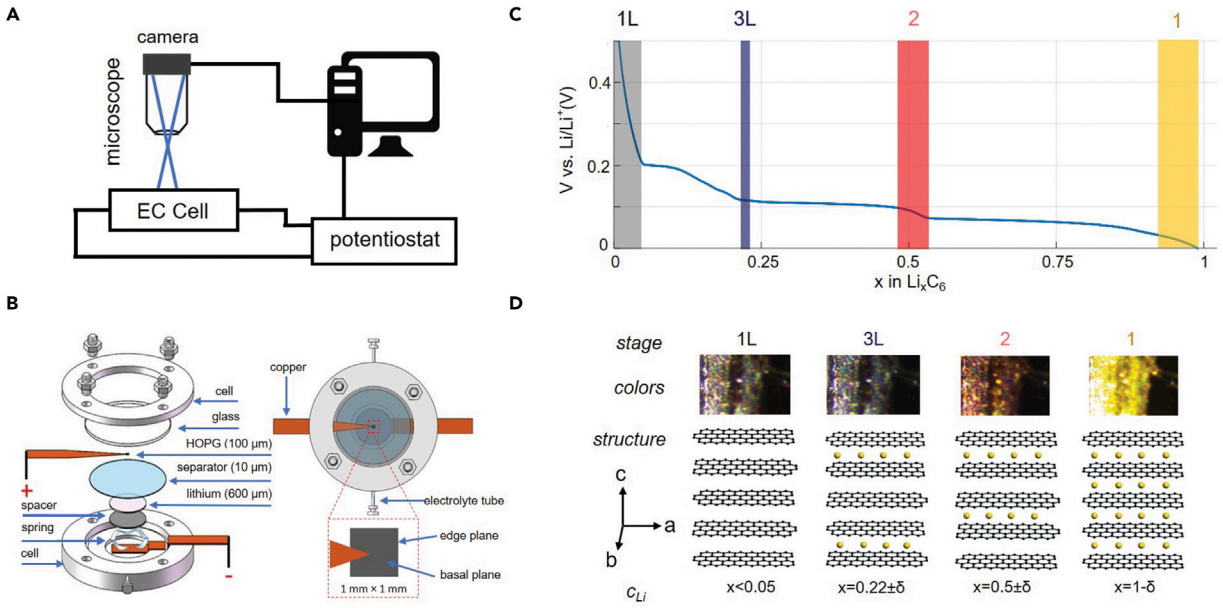

Figure 2. The Experimental Apparatus and Principle

(A) Schematic of the *in situ* experiment set-up; Li concentration in graphite and its voltage can be simultaneously monitored by charging/discharging with the potentiostat and concurrently recording with the camera.

(B) Schematic of the electrochemical cell; the cell enables collecting current from the a particle while exposing its basal surface to the camera for recording. The thickness of HOPG, separator, and lithium are shown.

(C) Typical voltage curve of micron-sized graphite during lithiation at quasi-equilibrium condition; the voltage curve is featured by three plateaus corresponding to 1L–4L, 3L-2 and 2–1 phase transformations. The solid-solution region of individual phases are marked by their corresponding colors. Stage 2L is not shown for simplicity. The number here refers to the number of graphene layers between the intercalated lithium layer. L refers to the liquid state, indicating the inserted lithium do not have any in plane order, i.e., they are distributed randomly in the interstitial spaces between graphene sheets. The details of the structures of these phases can be found in early work of Dahn [49] and Schweidler et al.[75]

(D) The images, structure, and Li concentration of different stages. Different stages have distinctive colors due to their unique electronic property. Stage 1L is dark gray, stage 4L and stage 3L are dark blue/purple, stage 2 is red and stage 1 is gold. Since the colors of stage 4L and 3L are hard to distinguish and the filling fraction difference between 1L and 4L is small, we only discuss stage 3L. The unique colors of Li-graphite intercalation compounds allow the monitoring of the spatial distribution of Li in graphite using optical microscopy. The concentration is from Schweidler et al.[50], δ refers to the range of solid solution.

except for 4L - 3L transition. The plated Li has a unique silver metal color.[19] Results of two representative graphite particles are given below, and more results are given in the Supplemental Information.

Lithiation

Li intercalation starts at 0.5 V (Figure 3A), predominantly at the edge plane.[51] The inserted Li primarily accumulates near the surface of the edge plane, indicated by the shallow penetration depth of the gold phase (stage 1) into the particle (Figures S1–S5). Phase separation is clearly observed during lithiation, when the local concentration enters the spinodal region for such a phase separating material (Video S1; Supplemental Information).[27,29] The presence of dark blue phase (stage 3L) and red phase (stage 2) is only transient. Gold phase (stage 1) forms almost immediately after the red phase (stage 2) likely due to a rapid increase of surface concentration. The co-existence of the gold phase (stage 1) and the black phase (stage 1L) is non-equilibrium phase separation. At the concentration of x = 0.21 (Figure 3C-6), the equilibrium state is stage 4L to stage 3L transformation (Figure 2C). From the penetration depth of the gold phase, the diffusion coefficient is estimated to be $D = \frac{L_p^2}{\tau_p} \approx 0.5(\pm 0.34) \times 10^{-8} cm^2/s$, consistent with the reported

Please cite this article in press as: Gao et al., Interplay of Lithium Intercalation and Plating on a Single Graphite Particle, Joule (2021), https://doi.org/10.1016/j.joule.2020.12.020

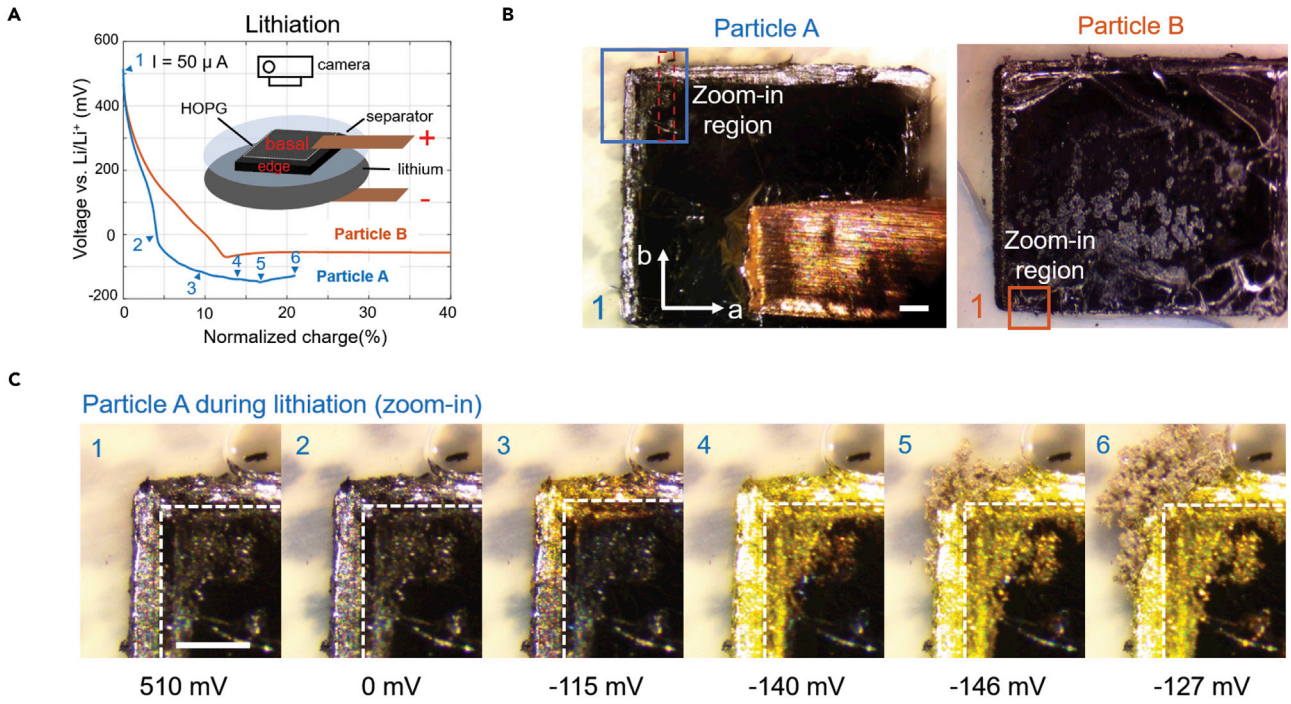

Figure 3. Voltage Profile and Optical Images during Lithiation

(A) Voltage profile. inset: the schematic of the HOPG/separator/Li sandwich inside the *in situ* electrochemical cell.

(B) The images of two representative particles before reduction. Scale bar, 100 μm. The solid box shows the regions for the zoom-in observation. The dashed red box shows the portion of image analyzed for comparison with theory. The Cu tape is under the particle for Particle B.

(C) Particle A during lithiation. The edge plane of the particle is not vertical (tilted) which allows the observation of the edge surface from above. The white dashed line marks the boundary between the basal plane and edge plane. Scale bar: 100 μm. No Li plating can be observed until all the edge surface is occupied by the gold phase. Videos are given in supplemental materials.

value of $0.2-10\times10^{-8}cm^2/s$.[52] Diffusion fails to remove the inserted Li promptly for the millimeter particle at this current, since diffusion time scale $\tau_D=\frac{R^2}{D}\approx\frac{0.5mm^2}{0.5\times10^{-8}cm^2/s}=0.5\times10^6$s is much larger than lithiation time scale $\tau_I=\frac{\rho VC_s}{I}=\frac{2.26g/cm^3\times0.1mm^3\times372mAh/g}{50\mu A}=4.8\times10^3$s,[26] which results in rapid accumulation of Li at the surface. As a result, the gold phase nucleates quickly before the red phase has had much time to propagate into the bulk of the particle.

Li intercalation preferentially occurs at the corner of the particle (Figure 3C) or any protruded debris (Figures S4 and S5), likely due to the higher surface/volume ratio. No Li plating can be observed when the voltage just drops below zero. Instead, we only observe Li plating shortly after the formation of the gold phase, which happens at a much lower voltage ($V\sim-0.15$ V versus Li/Li$^+$). There is a small voltage dip before Li plating starts (Figure 3A) due to the nucleation barrier (surface energy or residual stress of SEI[53,54]). Once Li plating initiates, the voltage curve stops decreasing and enters a plateau. To compare the rest and de-lithiation behavior of graphite particles at different amounts of plated lithium, the total passed charge during the lithiation is intentionally controlled. The voltage profile of particle B shares a similar trend with that of particle A, but they do not overlap. To explain such variation, the voltage curves of another three graphite particles at different currents are given in Figure S6. In the current range of 5–100 μA, a sharp transition between the voltage slope for Li insertion and the plateau for Li plating can be observed for every particle. Clear nucleation dip can be observed in some cases,

Please cite this article in press as: Gao et al., Interplay of Lithium Intercalation and Plating on a Single Graphite Particle, Joule (2021), https://doi.org/10.1016/j.joule.2020.12.020

e.g., 10 μA for particle J, but it is not obvious in other cases. Furthermore, the voltage profiles of seven different particles at 50 μA are plotted in Figure S7. The voltage profiles resemble the overall trend but do not overlap. Such discrepancy in voltage curves may arise due to variation in particle size and shape, as well as the different surface roughness introduced in the sample preparation process, (e.g., Figures S4 and S5), because nucleation is very sensitive to surface defects.[55,56] This kind of large variation is not common in a commercial graphite electrode, in which the presence of a large quantity of particles, $3.9\times10^7/cm^2$ for an electrode with 10 mg/cm^2 loading (assuming an average particle size of 3 μm), smooth out the random variations in size, shape, morphology and/or surface among particles. Statistical analysis of the results shows the nucleation barrier falls in -82.9 ± 75.3 mV and the critical capacity for nucleation falls in 12.2% $\pm$ 10.55% with 95% confidence. We disassembled some cells after charging and found that Li plating also occurs on the bottom side of the HOPG particle (Figure S8).

The intercalation involves the concurrent transfer of Li^+ and electron to the interstitial site in graphite. The availability of electrons cannot be rate-limiting because graphite remains semi-metallic/metallic during lithiation. However, the shortage of vacant sites due to surface saturation in graphite or shortage of Li^+ in the electrolyte may render the intercalation reaction difficult. The surface concentration depends on the balance between Li intercalation and solid diffusion of Li into the graphite bulk. Saturation happens when diffusion of Li is slower than the rate of Li intercalation into graphite. At the applied current ($\approx C/15$), the voltage can be approximated by (Supplemental Information):

$$V \approx -\frac{\mu_s}{e} + \eta_{int} \qquad \text{(Equation 1)}$$

in which μ_s and η_{int} are the chemical potential of intercalated Li at the edge surface and the overpotential of the intercalation reaction, respectively. The voltage drops sharply, instead of showing multiple voltage plateaus (cf. Figure 2C) due to the fast accumulation of Li at the edge surface. Such surface saturation impedes further intercalation due to the lattice crowding effect,[28] making Li plating kinetically favorable. At this C-rate, close to equilibrium behavior is expected for commercial graphite electrode because the graphite particle size (typically 0.1–10 μm) is much less than the diffusion penetration depth $L_p = \sqrt{Dt} = \sqrt{0.5(\pm0.34)\times\frac{10^{-8}cm^2}{s}\times15\times3,600\ s} = 156.7\pm63.8\ \mu$m. However, this is not the case for the millimeter HOPG particle used in our study. The large particle size renders it difficult for the inserted Li to reach the interior of the HOPG, leading to the accumulation of lithium near the surface, which triggers the phase separation observed in Figure 2. We will further discuss the size effect and the generalizability of the results to the commercial battery electrodes in the discussion. Ion transport in the electrolyte is not rate-limiting because the applied current density $J_{applied} \approx 1.25\ mA/cm^2$ is much smaller than the diffusion-limited current $J_{lim} = \frac{2zFcD_e}{(1-t_c)L} = \frac{2\times96,485\ C/mol\times1mol/L\times3\times10^{-6}cm^2/s}{0.6\times100\mu m} \approx 32.1\ mA/cm^2$. It influences the lithiation dynamics in the c-direction of the graphite particles to some extent (Figure S9) but does not alter the onset condition of Li plating (Figure S10).

Rest after Lithiation

Two different behaviors are observed during the rest after the partciles are lithiated and Li plating occurs(Figure 4, particle A versus B). For a particle with a small amount of plated Li (particle A, $\sim$ 6.5% normalized charge), the plated Li gradually disappears, leaving black floc-like residue (Figures 4D, 7–8, and S11). Meanwhile, the phase separation also disappears due to inward diffusion of Li (Figures 4D, 9–12;

Please cite this article in press as: Gao et al., Interplay of Lithium Intercalation and Plating on a Single Graphite Particle, Joule (2021), https://doi.org/10.1016/j.joule.2020.12.020

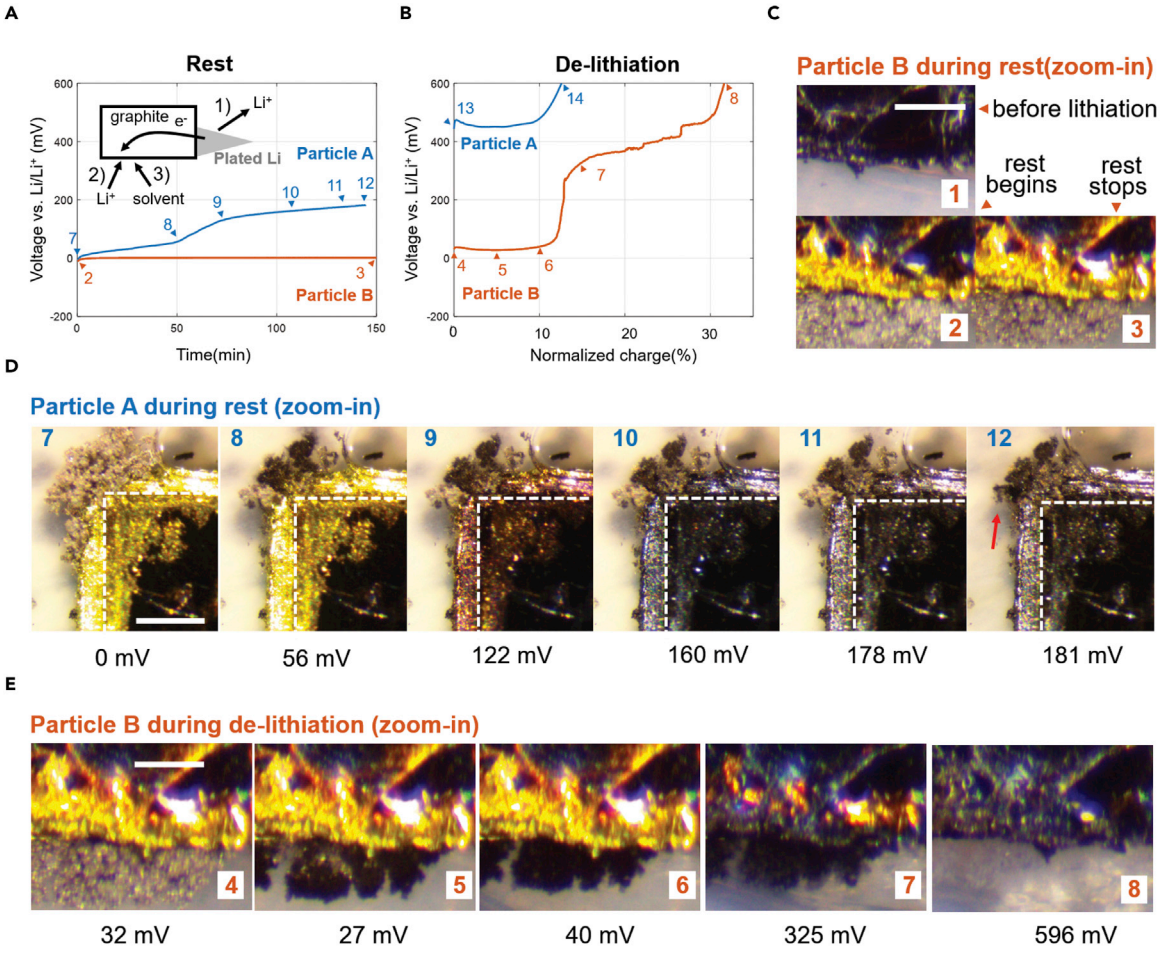

Figure 4. Voltage Profiles and Optical Images during Rest and De-lithiation

(A and B) Voltage profile during rest (A) and de-lithiation (B). inset: schematic of how the plated Li dissolves.

(C) Particle B during rest; scale bar, 100 μm.

(D) Particle A during rest; scale bar, 100 μm. Red arrow indicates the disappearance of the last active Li.

(E) Particle B during de-lithiation. Scale bar, 100 μm.

Video S2). The voltage stays on a plateau close to 0 mV initially (Figure 4A, 7–8 of particle A) but gradually increases due to the shrinking surface concentration after most deposited Li is dissolved ($V = -\frac{\mu_s}{e}$). Not all plated Li disappears during rest, which suggests that some of the deposited Li may have lost electrical connectivity with graphite (known as dead Li) (Figure 4D, 12). If a significant amount of Li is plated (particle B, 31% normalized charge), the metallic deposits do not completely dissolve during rest (Figure 4C), and the voltage remains at approximately 0 mV for the duration of the rest period (Figure 4A, particle B).

The disappearance of the plated Li can be understood by considering the chemical potential difference of the plated Li and the inserted Li in graphite (Figure 4A, inset). As the concentration of inserted Li at the graphite surface decreases due to inward diffusion, its chemical potential μ_s decreases, which creates a driving force between the plated Li and graphite edge surface. As a result, the plated Li dissolves and gives out electrons, and Li^+ from the electrolyte gets reduced and inserts into graphite. In other words, the plated Li forms a local short circuit with graphite. In addition to this electrochemical route, the disappearance of the plated Li can also occur through a

direct route in which the plated Li in contact with graphite can enter the graphite lattice. The continuing intercalation reaction is evidenced by the visible propagation of the gold phase into graphite during rest (Figure 4C), consistent with previous observations.[57] In addition to Li intercalation, solvent reduction may also happen to compensate the charge, if the SEI on graphite leaks electrons.

De-lithiation

After the rest, a positive (oxidizing) current is applied to remove the inserted and plated Li. If the amount of plated Li is small, most of the plated Li has already dissolved during the rest stage, except for any dead Li. As a result, the voltage profile resembles the de-lithiation of a normal graphite anode with no Li plating (Figure 4B, particle A), and the color change of the graphite particle is also negligible. If the amount of plated Li is large, it does not completely dissolve during rest. In this case, the de-lithiation voltage profile hovers around 20 *mV* (Figures 4B, 4–6 of particle B) as the plated Li shrinks and leaves behind a black floc-like residue (Figures 4E, 4–6). Once all electrically connected Li deposits have disappeared, normal graphite de-lithiation occurs and the voltage rises to another plateau at ca. 400 mV (Figures 4B, 7–8 of particle B).

The oxidation of the bulky silver lithium happens at a voltage below 100 *mV* (Figures 4A and 4B), where de-lithiation of graphite barely occurs. Once most of the bulky silver lithium has been dissolved, a black residue forms and the voltage rises above 100 mV, where de-lithiation of graphite occurs. We hypothesize the black residue is a micron-sized lithium covered by nanometer thick SEI. Bulky lithium metal shows a silver color. The color transforms to black, however, when the particle size reduces into micron regime. This happens because the dissolution of plated Li is intrinsically a corrosion reaction. During the transition of bulky lithium to the stacking of micron-particles of lithium, it loses the shining color. Once all bulk lithium has been transformed into micron-particles, the percolating pathway for electron conduction is significantly impaired since the particles are separated by the surface film, which is highly ionic conducting but poorly electronic conducting. Therefore, the oxidation of these small particles becomes kinetically difficult. They can still be oxidized if large overpotential is applied and mechanical contact is still maintained. The black residue on particle B finally dissolved when the voltage is raised to 600 *mV* (Figures 4E 7–8), which can be clearly seen in the supplemental video (Video S3). To summarize, the black residue can still be dissolved, despite more kinetically difficult, if their mechanical contact with the graphite is maintained. However, they become real dead lithium once their connection with graphite is cut during the dissolution if the root of the plated lithium gets dissolved first.

We did experiments on many particles with different amounts of lithium. All our observations fall into two groups: the first group, exemplified by particle A, shows complete lithium dissolution except for the dead lithium and disappearance of the phase separation in graphite particle during rest; whereas the second group, exemplified by particle B, shows the incomplete dissolution of the plated Li and a close to zero voltage during the entire rest. Inhomogeneity of the lithiation and de-lithiation of HOPG particles can be observed in some particles. For example, the non-lithiated region is sandwiched by two lithiated regions in Figures 4C and 4E. This inhomogeneity is likely due to the surface defects on the basal plane, which could be introduced in the sample preparation process. On particle B, there seem to be some line defects on the basal plane. These line defects create Li diffusion pathways on the surface. As a result, Li-rich gold phase forms along the lines, where other regions at the same distance from the reacting surface remain non-lithiated. Such line

Please cite this article in press as: Gao et al., Interplay of Lithium Intercalation and Plating on a Single Graphite Particle, Joule (2021), https://doi.org/10.1016/j.joule.2020.12.020

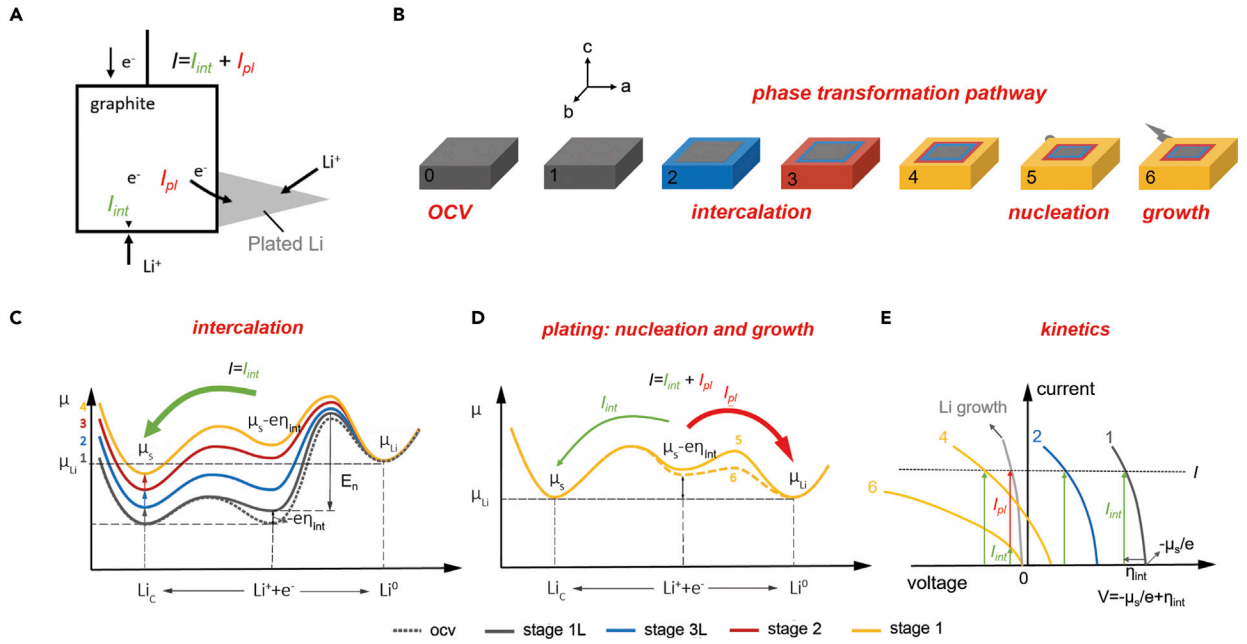

Figure 5. The Mechanism of Li Plating on the Graphite

(A) Competition between Li intercalation and plating during charging; I is total current, I_{int} is the current for Li intercalation, and I_{pl} is the current for Li plating.

(B) Schematic of the HOPG particle during lithiation.

(C and D) Reaction energy landscape before plating occurs (C) and after plating starts (D). μ denotes chemical potential (including electrostatic energy); the chemical potential of the reactants (Li^+ and e^-) and products (Li_C for intercalation and Li^0 for plating) are plotted against the reaction coordinate. Li_C refers to the inserted Li in graphite. μ_s is the chemical potential of the inserted Li at graphite surface. η_{int} is the overpotential for intercalation. E_n is the energy barrier for nucleation. μ_{Li} is the chemical potential of Li metal and equals 0 since Li metal is the reference. The voltage of graphite is $-\frac{\mu_s}{e}+\eta_{int}$, which equals $-\frac{\mu_s}{e}$ at open circuit ($I = 0$). The intercalation increases Li concentration at graphite surface c_s, leading to a series of phase transformation (1L-3L-2-1) and increase in μ_s.

(E) Kinetics of both reactions at different c_s. The I-V curves of Li insertion (dark gray, blue, and orange) and Li plating (light gray) are plotted. The schematic captures both the changing thermodynamics and kinetics of graphite during charging. Increasing c_s leads to increasing μ_s and less steeper I-V curve because the intercalation reactions become more difficult due to surface crowding. Once Li growth starts, $V = -\frac{\mu_s}{e}+\eta_{int} = -\frac{\mu_{Li}}{e}+\eta_{pl}$. Points 3 and 6 are not shown for simplicity.

defects can be step edges, which are commonly observed on cleaved HOPG basal plane.[58,59]

In summary, no Li plating can be observed when the voltage just drops below 0 *V*. Instead, significant Li plating occurs only after the graphite surface is saturated (after gold phase forms), and the onset of Li plating is accompanied by the switching of voltage curve from a decreasing ramp to a plateau. During rest, the plated Li gradually dissolves, and Li^+ ions continue to insert into graphite via a local self-discharge mechanism, relaxing toward the thermodynamically stable state. During this process, some plated Li is electrically disconnected from graphite during the dissolution and becomes inactive (dead Li). The voltage of the graphite will remain close to 0 *mV* until all active Li is dissolved. During de-lithiation, the dissolution of Li happens first, which is followed by the de-intercalation of graphite.

Physical Picture

To explain the above observations, we draw the competition of Li intercalation with Li plating (Figure 5A), the phase transformation pathway of the HOPG particle (Figure 5B), the energy landscape of the system (Figures 5C and 5D), and the associate kinetics (I-V curve) of both reactions (Figure 5E). SEI growth on graphite is neglected

Please cite this article in press as: Gao et al., Interplay of Lithium Intercalation and Plating on a Single Graphite Particle, Joule (2021), https://doi.org/10.1016/j.joule.2020.12.020

since the cell is pre-cycled to form SEI. Its formation on newly deposited Li metal is treated as a pure chemical reaction and neglected for simplicity. Therefore, there are two electrochemical reduction reactions taking place on the edge surface of the graphite particle during battery charging: Li intercalation (I_{int}) and plating (I_{pl}) (Figure 5A). The lithiation of graphite can be broken down into four regimes: *open circuit*, *Li intercalation*, *Li nucleation*, and *Li growth*.

(1) *Open circuit*: Before we apply any current, Li^+ and e^- are in equilibrium with inserted Li, denoted as Li_C (Figure 5C). The chemical potential of inserted Li at the graphite surface, μ_s, is much lower than the chemical potential of lithium metal μ_{Li} (V is much higher than 0 V, $V = -\frac{\mu_s}{e}$).

(2) *Li intercalation*: The system enters the second regime when a reduction current $I<0$ is enforced externally (charging). To drive the reaction, a negative overpotential occurs, raising the energy of $Li^+ + e^-$ (Figure 5C). The voltage now includes the overpotential required to drive the reaction ($V = -\frac{\mu_s}{e} + \eta_{int}$). Since μ_{Li} is much higher than $\mu_s - e\eta_{int}$ (i.e., $V>0$), plating is energetically not favorable (i.e., thermodynamically not possible). Therefore, only intercalation takes place. As more Li insert into graphite, the increasing surface concentration c_s induces a sequential phase transformation at the surface: 1L (gray) - 3L (blue) - 2 (red) - 1 (gold) (Figures 5B and 5C, 1–4).[34,49] Meanwhile, μ_s increases and the magnitude of the overpotential increases accordingly because the graphite surface becomes more crowded (Figure 5E).[29] As a result, the energy of the reactants increases, and the voltage decreases.

(3) *Li nucleation*: When the red or gold phase forms, Li plating may become *energetically* favorable ($\mu_s - e\eta_{int} > \mu_{Li}$, $V<0$) (Figures 5B and 5C, 3–4), but Li intercalation is still more favorable ($\mu_s < \mu_{Li}$). In addition, Li intercalation is *kinetically* more favorable since it does not need to overcome a nucleation barrier. The tipping point is the saturation of the graphite surface (Figures 5B and 5C, 5). This is becasue, first, Li plating becomes energetically equally favorable ($\mu_s = \mu_{Li}$) compared to Li intercalation. Second, Li intercalation becomes kinetically very difficult because there is no more available site in graphite for Li to occupy,[29] whereas Li plating becomes kinetically feasible because the nucleation barrier drops significantly due to the wetting of LiC_6 to Li.[60] As a result, the nucleation of Li metal starts, and V reaches its minimum.

(4) *Li growth*: Once nuclei forms, subsequent Li growth on the nuclei requires a much smaller activation energy than nucleation (Figures 5D, 6). Now the reduction reaction is dominated by the growth of Li metal (Figure 5E), and the intercalation only proceeds in a rate that compensates the inward diffusion of Li in graphite and maintain c_s unchanged. V rises due to the decreased overpotential, which finally reaches a plateau. Once Li plating starts, V is lower than than the equilibrium voltage for Li plating (0 V) due to the required overpotential. The voltage reflects the thermodynamics and kinetics of both reactions by $V = -\frac{\mu_{Li}}{e} + \eta_{pl} = -\frac{\mu_s}{e} + \eta_{int}$.

Theory

Building on the physical picture, we formulate a mathematical model, which predicts the coupled dynamics of Li-ion intercalation, phase separation in graphite, and Li metal nucleation and growth.[28] Here, we consider the intercalation of Li ions in a particle of volume V (in m^3) through reactive boundaries of total surface area, A (in m^2). The Li-ion concentration c (in mol/m^3) evolves according to mass conservation

Please cite this article in press as: Gao et al., Interplay of Lithium Intercalation and Plating on a Single Graphite Particle, Joule (2021), https://doi.org/10.1016/j.joule.2020.12.020

$$\frac{\partial c}{\partial t} = -\nabla\cdot\boldsymbol{j} = \nabla\cdot\left(\frac{D(c)c}{k_B T}\nabla\mu\right) \qquad \text{(Equation 2)}$$

where $\boldsymbol{j}$ is the diffusive flux defined in terms of the gradient of μ, the diffusional chemical potential, $D(c)$ is the tracer diffusivity that depends on species concentration, and k_B and T are the Boltzmann's constant and absolute temperature, respectively.[28,45,61] Ion intercalation is described by a boundary condition expressing mass conservation on the intercalation surfaces $-\boldsymbol{n}\cdot\boldsymbol{j} = R$, where $R(c,\eta_{int})$ is the intercalation rate, related to the intercalation current $i_{int} = eR$, and depends on the interfacial Li concentration c and local overpotential $e\eta_{int} = eV + \mu_s$.

The thermodynamically consistent modeling framework is based on the free energy functional:

$$G = \int_V \left(g_h(c) + \frac{1}{2}\kappa|\nabla c|^2\right) dV \qquad \text{(Equation 3)}$$

where g_h is the homogeneous free energy and κ describes the interfacial tension between the formed phases. Graphite is known to undergo multiple phase separations with increasing Li concentration. It is well-accepted that the inter- and intra-layer Li-Li interactions in graphite are different. To account for this effect, multi-variable concentration models have been developed.[27,42] Here, we follow a simpler approach that uses a reduced-order homogeneous free energy[27] that has been shown to quantitatively describe phase separation dynamics in commercial graphite electrodes.[34] The diffusional chemical potential, which controls the flux $\boldsymbol{j}$ and reaction rate R, is defined as the variational derivative of the free energy with respect to the concentration field, $\mu_s = \delta G/\delta c$. The tracer diffusivity $D(c)$ is obtained by fitting to the results of *ab initio* simulations.[52]

For the intercalation rate, we use the theory of coupled ion-electron transfer (CIET) kinetics,[45,46] which unifies the theory of electron transfer[62,63] with the non-equilibrium thermodynamics of ion transfer in condensed phases.[28,43] Using a simple formula for the Marcus-Hush-Chidsey electron transfer rate,[63] the CIET rate can be cast in the form[46]:

$$i_{int} = k_{0,int}(1-c)\sqrt{\pi\tilde{\lambda}}\left(\frac{c_l}{1+e^{\tilde{\eta}_f}} - \frac{c}{1+e^{-\tilde{\eta}_f}}\right) erfc\left(\frac{\tilde{\lambda} - \sqrt{1+\sqrt{\tilde{\lambda}}+\tilde{\eta}_f^2}}{2\sqrt{\tilde{\lambda}}}\right) \qquad \text{(Equation 4)}$$

where $k_{0,int}$ is an overall rate constant, c_l is the normalized electrolyte concentration, $\tilde{\eta}_f = e\eta_{int}/k_B T + ln(c_l/c)$ the formal overpotential scaled to the thermal voltage $k_B T/e$ and $\tilde{\lambda} = \lambda/k_B T$ is the scaled reorganization energy. At high overpotential, CIET predicts a reaction-limited current, which decreases with the concentration of available vacancies $(1-c)$ in the intercalation material.[46] In contrast to empirical Butler-Volmer kinetics,[28] this behavior favors the parasitic side reaction of Li plating.

The applied current I is shared between the plating and intercalation reactions:

$$I = \int i_{pl}\, dA_{Li} + \int i_{int}\, dA \qquad \text{(Equation 5)}$$

where the first integral is over the active surface of the Li metal film and the second over the graphite particle surface. When the surface of the particle is almost fully lithiated ($c_s \to 1$), intercalation becomes difficult due to the surface crowding effects.[28,46] For the applied current to be sustained, though, the overpotential of the intercalation reaction η_{int} makes the voltage drop below the nucleation voltage

Please cite this article in press as: Gao et al., Interplay of Lithium Intercalation and Plating on a Single Graphite Particle, Joule (2021), https://doi.org/10.1016/j.joule.2020.12.020

$-V_{0,n}$ and triggers Li metal nucleation on the graphite surface. After the deposition of the first Li metal, the overpotential of Li plating η_{pl} leads to $\int i_{pl}\, dA_{Li} \simeq I$.

Despite the experimental observations (Figure 3) showing that Li metal exhibits complicated morphologies of mossy or dendritic growth,[19,54,64] our goal here is to capture the total amount of deposited Li metal per area of the graphite edge surface in a simple macroscopic model. In particular, we equate the growth rate of deposited metal with the microscopic current density $i_{pl,m}$ over the curved area A_{Li} of growing and merging nuclei, as well as the mean current density i_{pl} projected on the underlying planar area A_p of the graphite surface:

$$\frac{1}{\Omega}\frac{dV_{Li}}{dt} = A_{Li}\frac{i_{pl,m}}{e} = A_p\frac{i_{pl}}{e} \qquad \text{(Equation 6)}$$

which is the mass conservation for $n_{Li} = V_{Li}/\Omega$, where V_{Li} and Ω are the total and molar volumes of Li metal, respectively. For the growth of isolated hemispherical nuclei, we have the scaling, $A_{Li} = A_{nuc}(V_{Li}/V_{nuc})^{\beta}$ with $\beta = 2/3$, where $A_{nuc} = NA_{0,nuc}$ and $V_{nuc} = NV_{0,nuc}$ are the initial area and volume of N nuclei. The thermodynamic stability of a nucleus that deposits on an electrically charged substrate is determined by the bulk free energy of transformation, both chemical and electrical, and the surface tension contributions. For a single, isolated, hemispherical electrodeposit, the kinetic critical radius corresponding to the case where the Laplace pressure balances the applied overpotential is given by Ely and García[65]:

$$r^*_{nuc} = \frac{2\gamma\Omega}{zF\eta_{pl}} \qquad \text{(Equation 7)}$$

As the nuclei merge and coarsen, their number will decrease, and the exponent β will also decrease, although typically not reaching the dense-film limit $\beta = 0$ (constant area). For an observed plating onset overpotential $\eta_{pl} \sim 0.15$ V versus $Li/\,Li^+$ in our experiments (Figure 3A), the kinetic critical radius r^*_{nuc} is approximately 0.75 nm. $A_{0,nuc}$ and $V_{0,nuc}$ for a growing hemisphere at critical radius subsequently can be calculated using $A_{0,nuc} = 2\pi r^{*2}_{nuc}$ and $V_{0,nuc} = (2/3)\pi r^{*3}_{nuc}$.

For the rates of microscopic and macroscopic Li plating, $i_{pl,m}$ and i_{pl}, we assume symmetric ($\alpha = 0.5$) Butler-Volmer kinetics[28] (neglecting curvature effects on the overpotential[44]), which implies the exchange currents are related as $A_{Li}i_{0,pl,m} = A_p i_{0,pl}$. Direct observation of a single hemispherical growing nucleus of Li metal on gold, under constant voltage, has shown that the microscopic current density decays as $i_{0,pl,m} \sim t^{-1/2}$, due to diffusion limitation of Li ions across a rapidly growing layer of SEI on the Li metal exposed to the unstable organic electrolyte.[54] Similar passivation of nuclei by SEI should occur for metal growth on graphite, and this effect approximately cancels the initial area growth, $A_{Li}/A_p \sim t^{\beta}$, for a constant macroscopic current density, $V_{Li} \sim t$. As such, we assume the macroscopic exchange current $i_{0,pl}$ is approximately constant.

For Li plating to occur, the voltage of the graphite particle needs to overcome a nucleation barrier V_n, Figure 5. To account for this phenomenon, we modify the overpotential of the Li plating reaction as $\eta_{pl} = \frac{\mu_{Li}}{e} + V - V_n$, which implies that for the plating current i_{pl} to be non-zero the voltage V has to overcome the nucleation voltage V_n. The reference chemical potential for our system is μ_{Li} , and thus we set its value equal to zero. After the first nuclei are formed the plating current concentrates on them, and thus there is no additional energy cost to grow the deposited film of Li metal. To achieve that, we postulate $V_n = V_{0,n}exp(-V^2_{Li}/2V^2_{nuc})$, which vanishes after $V_{Li} \gg V_{nuc}$. The functional form of $V_{0,n}$ can be expressed by other

Please cite this article in press as: Gao et al., Interplay of Lithium Intercalation and Plating on a Single Graphite Particle, Joule (2021), https://doi.org/10.1016/j.joule.2020.12.020

mathematical descriptions, although here we use the Gaussian approximation for numerical purposes.

The computational model corresponds to one-dimensional slice of the graphite particles, Figures 3 and 4. For discretizing Equation 2 we use second-order finite volumes.[66] Specific details on the constitutive relations for the non-linear diffusivity, the intercalation rates, the fitting procedure for $i_{0,pl}$, as well as the thermodynamic, transport, and reaction parameters are given in detail in the Supplemental Information. For the intercalation model, we consider $k_{0,int} = 1$ A/m^2,[27] and the reorganization energy $\lambda = 5k_BT$, which is estimated from experiments on other intercalation compounds (D.F., T.G., and M.Z.B., unpublished data).[46] Finally, the nucleation barrier for Li plating on graphite is estimated to be $V_{0,n} \sim -0.15$ V versus Li/Li$^+$, by fitting the Li plating model (nucleation and kinetics) to the simultaneous measurements of video images (concentration profiles) and voltage, while keeping the other parameters (for intercalation and transport) fixed at values determined from previous studies. This approach is especially important for complex heterogeneous processes, such as electrodeposition coupled with intercalation in a phase separating substrate, which is more complicated that traditional electrodeposition processes on impermeable metal electrodes (such as Li on Cu). This value is specific to particle A in Figure 3A due to the particle-by-particle variation in size, shape, morphology and/or surface, but this method can be generalized to any other particle.

Model Validation and Predictions

We test our predictions on Li plating by fitting the Li plating exchange current density $i_{0,pl}$ using the experimental voltage-charge data of the lithiation case of Figure 3. The validation of our fitting is based on the extracted concentration profiles of the intercalated Li ions, as well as the total amount of plated Li on the particle at the end of the experiment, Figure 6A. The fitted value for the macroscopic exchange current (per projected area) for Li plating on the graphite edge plane is $i_{0,pl} = 2.2$ A/m^2, which takes into account direct observation of the plating area.

Figure 6B shows our model predictions, where the thick dashed lines (in black) correspond to the experimentally extracted profiles of the intercalated and plated Li. The computational results are shown with the colored areas. Our simulations demonstrate the predictability of the phase-field model for graphite as it can qualitatively capture the observed Li-ion concentration evolution inside the particle. Additionally, Figure 6D demonstrates the fitted and experimentally observed voltage versus charge profiles. Finally, Figure 6E depicts the the model predictions of the voltage V and surface concentration c_s under de-lithiation.

The model can predict the onset of Li plating and the correct value of the nucleation voltage. As discussed in Figure 5 based on the experimental observations, Li plating occurs only when the surface of graphite becomes saturated by the inserted Li ions. Figure 6D demonstrates the evolution of the surface concentration as a function of the average Li fraction in the graphite particle. Our calculations show that when the surface concentration c_s becomes 1 the nucleation barrier is exceeded. At this point, the intercalation current I_{int} drops sharply, and the plating current I_{pl} increases significantly and dominates the applied current I.

The most widespread approach to model Li intercalation in graphite combines Butler-Volmer kinetics with Fick's law for diffusion with concentration-dependent diffusivities. Our experiments, though, showed that phase separation affects the concentration at the reaction boundary of the graphite particle, causing abrupt changes

Please cite this article in press as: Gao et al., Interplay of Lithium Intercalation and Plating on a Single Graphite Particle, Joule (2021), https://doi.org/10.1016/j.joule.2020.12.020

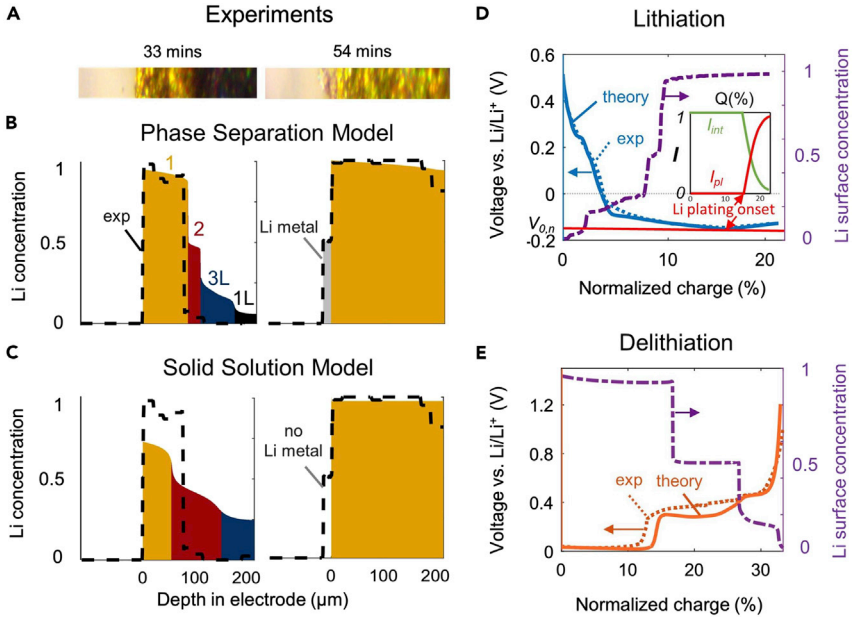

Figure 6. Theory and Simulation

(A) Images of graphite particle used to extract the Li concentration and Li plating profiles.

(B and C) Model predictions of Li concentration profiles compared with experimental data.

(B) Predictions using the phase separation model.

(C) Predictions using the solid-solution model. The model considering phase separating in graphite can capture the abrupt increase of c_s when it enters spinodal region, and therefore gives accurate prediction of Li onset. In contrast, the solid-solution model underestimates c_s and fails to predict the onset of Li plating.

(D and E) Voltage and predicted Li surface concentration during lithiation and de-lithiation of graphite. Inset in (D): current for Li plating and intercalation in the dimensionless form. The onset of Li plating is marked by the red arrow. The blue, purple, and orange arrows are used to indicate which y axis the curve corresponds to.

once the concentration at the boundary enters the spinodal region. In order to show that traditional diffusion models cannot capture this phenomenon, we perform solid-solution calculations for the same conditions as in Figure 6C. It is clear in Figure 6C that the surface concentration of the intercalated Li ions does not increase as fast with the solid-solution model as with the phase separation model. The result of such delay is reflected in the absence of plated Li.

Using classical nucleation theory,[44] we can estimate the initial number of nucleated sites. The surface tension of Li metal with organic electrolytes is around $\gamma \simeq 0.49$ J/m^2[12] and results in a critical hemisphere radius of $r_{nuc} \simeq 0.75$ nm ($A_{0,nuc} = 2\pi r_{nuc}^2$ and $V_{0,nuc} = (2/3)\pi r_{nuc}^3$). For the experimentally observed projected area A_p, we find the initial number of Li metal nuclei to be $N \simeq 5.7 \times 10^8$. This value was used in the evaluation of the Li plating model, Equation 6 and in the initial condition for the volume of Li metal $V_{Li,0}$.

DISCUSSION

In summary, Li plating on a single graphite particle is triggered when graphite surface saturates ($c_s \rightarrow 1$) and Li-ion intercalation is blocked. Li plating is thermodynamically possible when $V<0$, but it is not kinetically favored until graphite surface is saturated. This kinetic disadvantage of plating compared to intercalation is due to (1) Li nucleation barrier,[54] captured by our theory, and (2) non-wetting property

Please cite this article in press as: Gao et al., Interplay of Lithium Intercalation and Plating on a Single Graphite Particle, Joule (2021), https://doi.org/10.1016/j.joule.2020.12.020

of the Li-poor phase (Li_xC_6, $x<1$) to Li metal.[53,60] The saturation renders the graphite edge surface wettable to Li metal and meanwhile significantly impedes intercalation, making Li plating kinetically more favorable than intercalation. As a result, Li nucleation occurs, followed by subsequent Li metal growth.

The saturation of graphite surfaces can happen in two scenarios. Under quasi-equilibrium condition (small current, $\tau_D \ll \tau_l$), the lithiation of graphite proceeds via an intercalation wave mechanism, and surface saturation occurs only when the particle is fully lithiated. Under diffusion-limitation condition (large current, $\tau_D \gg \tau_l$), however, surface saturation can happen before the particle is fully filled, as the shrinking-core phase separation results in the piling up of inserted Li at the surface.[26]

Our analysis shows the solid diffusion limitation mechanism can explain the Li plating observed in our experiments. The effect of electrolyte transport is negligible since the applied current density $J_{applied}$ is much smaller than the diffusion limiting current J_{lim}. In fact, the saturation of graphite surface ($c_s \rightarrow 1$) always proceeds depletion of Li ions in the electrolyte ($c_l \rightarrow 0$) for a single particle electrode given the much higher diffusivity of Li ions in the electrolyte. For this reason, diffusion-limited aggregation is not responsible for the observed Li plating on the single graphite particle. However, this argument does not apply for a porous electrode, becasue the effective diffusivity is significantly compromised by the tortuous pores and reactions within the porous electrode expedite ion depletion, especially on the current collector side.[35] The competition between Li plating and Li intercalation in a porous electrode is beyond the scope of the current work due to heterogeneities in multiple length scales.[42] However, we believe the proposed diffusion-limited aggregation mechanism is not likely to account for Li plating in a porous electrode. In a porous electrode, Li plating is observed on the separator side whereas ion depletion happens on the current collector side,[33,35] which contradicts the prediction of diffusion-limited aggregation mechanism that dendrite growth initiates at zero salt concentration.[19]

The physical picture discussed above also explains the large negative voltage tolerance of single graphite particles without Li plating. Because V depends on both the surface chemical potential of Li in graphite and the voltage loss of reaction and other kinetic processes (e.g., diffusion and migration), it can be quite negative before graphite surface saturates. For this reason, V is not a suitable criterion for determining the onset of Li plating. In fact, V is always negative when graphite surface saturates ($\mu_s = 0$ and $\eta_{int} < 0$), which makes it only a necessary condition for Li plating. The sufficient condition for Li plating is $c_s \rightarrow 1$.

In addition to the fundamental knowledge, the observations on the HOPG particles are also relevant for commercial graphite electrode. In real graphite electrode, the onset of Li plating is a highly localized event, i.e., it initiates from a local spot in the porous graphite electrode and then propagates. Electrode-scale studies have revealed reaction heterogeneity among particles is highly correlated with the likelihood of Li plating,[30,32–34,37]but it remains unclear how Li plating occurs locally. Different hypotheses exist in literature regarding the onset condition of Li plating on graphite (Figure 1). However, no real-time experiment evidence at the particle scale is reported to test them. Our study fills this knowledge gap by focusing on the Li insertion, graphite phase transition, and Li plating dynamics of a single particle, using *in situ* experiment to monitor the Li concentration in graphite and the voltage.

Please cite this article in press as: Gao et al., Interplay of Lithium Intercalation and Plating on a Single Graphite Particle, Joule (2021), https://doi.org/10.1016/j.joule.2020.12.020

At first glance, the HOPG particle may seem too big to be representative of graphite particles used in the commercial electrodes. However, the experimental conditions are chosen to reflect the working condition of commercial graphite electrode under fast charge. More specifically, the current density per reaction area of the HOPG particle is in the same range as that of graphite particles in the commercial electrodes. Since graphite has a layered structure and insertion primarily happens at the edge plane, the current density per edge plane area is a better parameter than C-rate to characterize the lithiation dynamics. It appropriately accounts for the reaction rate at the active crystal plane and the resulted anisotropic lithiation dynamics along the *ab* plane. For a typical HOPG particle operating at 10–100 μA in this study, the current density per edge area is 1.25–12.5 mA/cm^2, which is representative of the 0.83–15.1 mA/cm^2 current density on graphite particles in commercial battery under 10 min fast charging (Supplemental Information). In fact, our observation that onset of Li plating is triggered by graphite surface saturation is consistent with a recent discovery of Li plating heterogeneity in a commercial battery.[2]

Since surface saturation triggers the onset of Li plating, its forecast relies on accurate prediction of concentration profile within graphite particles, especially surface concentration. The solid-solution model that use Fickian diffusion tends to underestimate the surface concentration because of the difficulty in maintaining high concentration gradient between two regions due to the high driving force for diffusion,[14,34] and thus underestimate the risk of Li plating. Therefore, phase transformation of graphite needs to be taken into account for predicting Li plating,[26,27,36] especially when less data are available for the calibration. Moreover, it is also crucial to capture the suppression of the intercalation reaction due to lattice saturation, as predicted by CIET theory.[28,43,45,46]

The fitted value, $i_{0,pl} = 2.2\ A/m^2$, is likely the most accurate to date for plating on graphite, since it reflects direct visualization of the active area for metal growth, as well as coupling to observed graphite phase transformations through a previously validated intercalation model with minimal extra fitting. For Li growth on carbon electrodes,[14,40,54] the reported literature values for $i_{0,pl}$ range from 10^{-3} to 10^2 A/m^2, which indicate the large uncertainty that exists on the kinetics of Li plating. Indeed, the microscopic physics have complicated effects on the macroscopic electrodeposition kinetics. The (de)solvation effects of Li ions may affect the energy barrier, while the evolving surface energy introduces an additional overpotential that decays with time with decreasing curvature as nuclei grow and merge. The irreversible side reaction of rapid SEI growth on freshly exposed metal tips passivates the surface and decreases the microscopic rate with square-root scaling in the limit of Li-ion transport limitation within the growing SEI layer.[54] Including this dependency only, we find $i_{0,pl,m} \approx 7 \times 10^3 \sqrt{t_{nuc}/t}\ A/m^2$, where t_{nuc} is the time to form a critical nucleus, which is consistent with the microscopic observed rate of hemispherical growth.[54] Together with our macroscopic observations, a quantitative picture of the reaction kinetics of Li plating on graphite begins to emerge.

The nucleation barrier to form Li metal should be very large until graphite surface saturates due to dewetting of graphite to Li metal.[53,60] This behavior can be described by our phenomenological model by including a concentration dependence on $V_{0,n}$ such that $V_{0,n} \rightarrow -\infty$ for $c_s \rightarrow 0$ and $V_{0,n} \rightarrow -0.15$ V for $c_s \rightarrow 1$. The relatively large value of $V_{0,n}$ may also be consistent with metal nucleation controlled by microscopic fracture and penetration of the pre-existing SEI layer on graphite.[54,64]

To estimate the initial total number of Li metal nuclei, we neglect SEI passivation and use classical nucleation theory with the surface tension measured for Li metal

Please cite this article in press as: Gao et al., Interplay of Lithium Intercalation and Plating on a Single Graphite Particle, Joule (2021), https://doi.org/10.1016/j.joule.2020.12.020

droplets in organic electrolytes,[12,67] in contrast to the the values used in most of the literature, based on estimates from aqueous metal plating experiments.[44,68] Based on the assumption of an initial layer of Li metal nuclei with the experimentally observed plated area A_p on graphite particles, we estimate the total number of nuclei as $N \sim 5 \times 10^8$. However, we should not interpret the result of classical nucleation theory strictly, due to the presence of SEI growth on both the graphite edge plane and the freshly exposed Li metal.

Our findings have direct implications for designing graphite electrodes with low risk of Li plating and capable of fast charging. Li plating occurs when graphite surface saturates and blocks further intercalation. Such saturation can happen much earlier before complete filling if solid diffusion of Li is slow. Therefore, reducing diffusion time inside graphite particles can be effective in enhancing the charging performance. Using the obtained diffusivity in this work $0.5(\pm 0.34) \times 10^{-8} \mathrm{cm}^2/\mathrm{s}$, the upper bound of particle size capable of DOE's 10 min charging goal is $R_c = \sqrt{Dt} = 16.1 \pm 6.3\ \mu\mathrm{m}$, in excellent agreement with previous experiment results in thin electrodes.[69] It should be noted though, the charging performance deteriorates significantly when the electrode thickness increases,[35] highlighting the importance of electrolyte transport. The ion depletion and concentration polarization in the depth direction of such thick electrode is well understood.[35,70] However, how electrolyte transport in the three dimensional structures affect the competition between Li plating and ion intercalation is yet to be elucidated.[37]

The results of the present work provide useful insights on battery management. Since diffusion can be facilitated by increased temperatures, warming up the battery is known to effectively enhance charging capabilities.[71] Optimization of the charging protocol can also be useful if the surface saturation can be delayed. Previous studies, though, require the voltage of the battery to be strictly positive during the optimization,[72] which is a very conservative criterion and may lead to sub-optimal charging protocol. Additionally, our results provide insights for detecting Li plating and fault diagnosis in battery management. The voltage plateau of Li dissolution can be used to signal Li plating during battery relaxation and discharge, but the voltage plateau of Li plating is not likely to be observed during battery charging because of the fixed cutoff voltage. In fact, recent experiment studies have observed the appearance of a short plateau on the rest and discharge voltage curve if Li plating happens in the preceding charging cycle,[15,73] and non-destructive technique for Li detection was proposed based on the observation.[74]

The role of solid diffusion limitation on reaction kinetics is general for any insertion material, whenever the rate of insertion overwhelms the diffusion of the inserted ions.[26] The concentration gradient causes a sharp voltage drop, which leads to low material utilization for potentiostatic operation or parasitic side reactions for galvanostatic operation. The triggering of Li plating, as one such parasitic reaction due to surface saturation, is also likely to happen in other anode materials, such as Si, Sn, Al, anatase, and titanate.

Finally, we want to discuss briefly the strength and limitation of the optical microscopy technique for studying graphite anode. Optical microscopy is a powerful tool for *in situ* experiments due to its high spatial (1 μm) and temporal (1 s or higher) resolution, but such analysis is limited to the surface due to the opacity of graphite. In this work, basal plane imaging qualitatively shows how the Li intercalation couples with phase separation. Quantitative analysis needs to consider the concentration gradient in the c-direction of graphite lattice, which will be the topic of future research.

Please cite this article in press as: Gao et al., Interplay of Lithium Intercalation and Plating on a Single Graphite Particle, Joule (2021), https://doi.org/10.1016/j.joule.2020.12.020

Conclusions

In conclusion, motivated by the need of addressing Li plating problem on graphite anode in Li-ion batteries, we examined the competition of Li plating and insertion using a single HOPG particle as the model system and studied the fundamental mechanism of Li plating. Using *in situ* optical microscopy, we concurrently monitored the dynamics of Li insertion and phase transition of graphite and its voltage and revealed the coupled intra-particle phase transformation and Li plating. We found that Li plating occurs on fully lithiated surfaces along the edge plane, and the onset voltage is much below 0 V versus Li/Li^+. Such observations were rationalized by examining the energetics and kinetics of the intercalation and plating reactions. Based on the experimental observations, we revealed that solid diffusion limitation leads to the saturation of graphite particle surface, which further triggers Li plating on the edge plane. Based on our mechanistic understanding on Li plating, we developed a Li plating model to predict both its onset and growth and demonstrated the importance of modeling the phase separation to predict the onset of Li plating.

Our findings shed light on the tolerance of graphite to large negative voltage before Li plating occurs and reveal the important physics that governs Li plating phenomena in graphite particles during battery charge. The fundamental insights gained at the particle scale lays the foundation for future work at the porous electrode scale by revealing the local interplay between Li plating and intercalation. It also provides a valuable tool to prevent Li plating on the systems level by enabling precise modeling and prediction of Li plating. The knowledge also shed light on design principle of graphite electrode and algorithm for battery operation optimization to achieve extreme fast charging without compromising battery safety and durability.

EXPERIMENTAL PROCEDURES

Resource Availability

Lead Contact

Further information and requests for resources and materials should be directed to and will be fulfilled by the Lead Contact, Martin Bazant (bazant@mit.edu).

Materials Availability

This study did not generate new unique materials.

Data and code availability

The data supporting the findings of this study are available within the main text and the Supplemental Information. More detailed data and the MATLAB code used for processing/analysis can be made available upon request to the corresponding author.

System preparation and Materials

The HOPG particle was bought from Sigma-Aldrich. The as-received HOPG foil is 10 mm × 10 mm × 2mm. It was peeled into thinner foil (100–200 μm) with Scotch tape and then cut by a razor blade to small square pieces of approximately 1 mm × 1 mm. A mini tri-layer battery was made by stacking the selected particle, a separator (MTI), and a Li chip (MTI) together, with the particle's basal plane facing up and its edge plane facing sideways. A copper cantilever was used as the current collector. The mini tri-layer battery was then loaded into the customized electrochemical cell, in which a quartz window is installed above the HOPG particle for *in situ* optical observation. After this, the electrolyte, 1 M $LiPF_6$ in EC/DEC = 50/50 (v/v) (Sigma-Aldrich), is injected into the cell with the tube on the side of the cell. During the

experiment, the HOPG particle was used as the working electrode and Li metal as the counter and reference electrodes. All the voltage values were referenced to Li/Li^+. The particle was pre-cycled at C/15 between 1.0 and 0 V for one cycle to form SEI. The effect of any subsequent SEI growth on graphite is neglected in this study. During lithiation, a negative current was applied until the voltage drops below zero and reaches a plateau. During de-lithiation, a positive current was applied until the voltage reached 1.0 *V*. The delivered charge was normalized by the theoretical capacity of the particle. The experiment was conducted at room temperature. The lab was regulated by a central air conditioner and the temperature is set to be 72°F (22.2°C). The customized electrochemical cell was made of PTFE.

Image Processing

Image processing is performed by extracting a small vertical slice (approximately 50 × 500 pixels in dimension) from the top left of the particle of Figure 3. The jagged edge slope of the HOPG particle is removed digitally to prevent erroneous readings from image processing. The final snipped image is contrast-enhanced and then processed using MATLAB Image Processing Toolbox, to convert the observed colors on graphite to a time-dependent concentration map. We use this concentration profile used to compare against the theoretical predictions our model.

SUPPLEMENTAL INFORMATION

Supplemental Information can be found online at https://doi.org/10.1016/j.joule.2020.12.020.

ACKNOWLEDGMENTS

This work was supported by the Toyota Research Institute through D3BATT: Center for Data-Driven Design of Li-Ion Batteries.

AUTHOR CONTRIBUTIONS

T.G. and Y.H. contributed equally to this work. T.G. and M.Z.B. conceived and designed this study. T.G. designed and performed the experiment with Y.H. T.G., T.Z., and D.F. developed the physical picture based on the results. S.D., D.F., T.Z., and M.Z.B. developed the mathematical model. S.D. performed the simulations and fitting to experimental data. T.G., S.D., D.F., and M.Z.B. prepared the manuscript and made the final edits. M.Z.B. is the lead contact of this work.

DECLARATION OF INTERESTS

The authors declare no competing interests.

Received: August 9, 2020
Revised: September 3, 2020
Accepted: December 18, 2020
Published: January 22, 2021

REFERENCES

1. Feng, X., Ouyang, M., Liu, X., Lu, L., Xia, Y., and He, X. (2018). Thermal runaway mechanism of lithium ion battery for electric vehicles: a review. Energy Storage Mater. *10*, 246–267.

2. Tanim, T.R., Shirk, M.G., Bewley, R.L., Dufek, E.J., and Liaw, B.Y. (2018). Fast charge implications: pack and cell analysis and comparison. J. Power Sources *381*, 56–65.

3. Ahmed, S., Bloom, I., Jansen, A.N., Tanim, T., Dufek, E.J., Pesaran, A., Burnham, A., Carlson, R.B., Dias, F., Hardy, K., et al. (2017). Enabling fast charging –a battery technology gap assessment. J. Power Sources *367*, 250–262.

4. Waldmann, T., Hogg, B.-I., and Wohlfahrt-Mehrens, M. (2018). Li plating as unwanted side reaction in commercial li-ion cells– a review. J. Power Sources *384*, 107–124.

5. Petzl, M., Kasper, M., and Danzer, M.A. (2015). Lithium plating in a commercial lithium-ion battery– a low-temperature aging study. J. Power Sources *275*, 799–807.

6. Attia, P.M., Das, S., Harris, S.J., Bazant, M.Z., and Chueh, W.C. (2019). Electrochemical kinetics of sei growth on carbon black: part I. Experiments. J. Electrochem. Soc. *166*, E97–E106.

7. Das, S., Attia, P.M., Chueh, W.C., and Bazant, M.Z. (2019). Electrochemical kinetics of sei growth on carbon black: Part II. Modeling. J. Electrochem. Soc. *166*, E107–E118.

8. Dubarry, M., Liaw, B.Y., Chen, M.-S., Chyan, S.-S., Han, K.-C., Sie, W.-T., and Wu, S.-H. (2011). Identifying battery aging mechanisms in large format li ion cells. J. Power Sources *196*, 3420–3425.

9. Huang, W., Attia, P.M., Wang, H., Renfrew, S.E., Jin, N., Das, S., Zhang, Z., Boyle, D.T., Li, Y., Bazant, M.Z., et al. (2019). Evolution of the solid–electrolyte interphase on carbonaceous anodes visualized by atomic-resolution cryogenic electron microscopy. Nano Lett. *19*, 5140–5148.

10. Agubra, V., and Fergus, J. (2013). Lithium ion battery anode aging mechanisms. Materials *6*, 1310–1325.

11. Han, X., Ouyang, M., Lu, L., Li, J., Zheng, Y., and Li, Z. (2014). A comparative study of commercial lithium ion battery cycle life in electrical vehicle: aging mechanism identification. J. Power Sources *251*, 38–54.

12. Lu, Y., Tu, Z., and Archer, L.A. (2014). Stable lithium electrodeposition in liquid and nanoporous solid electrolytes. Nat. Mater. *13*, 961–969.

13. Li, Z., Huang, J., Yann Liaw, B.Y., Metzler, V., and Zhang, J. (2014). A review of lithium deposition in lithium-ion and lithium metal secondary batteries. J. Power Sources *254*, 168–182.

14. Arora, P., Doyle, M., and White, R.E. (1999). Mathematical modeling of the lithium deposition overcharge reaction in lithium-ion batteries using carbon-based negative electrodes. J. Electrochem. Soc. *146*, 3543–3553.

15. Uhlmann, C., Illig, J., Ender, M., Schuster, R., and Ivers-Tiffée, E. (2015). In situ detection of lithium metal plating on graphite in experimental cells. J. Power Sources *279*, 428–438.

16. Shkrob, I.A., Rodrigues, M.-T.F., Dees, D.W., and Abraham, D.P. (2019). Fast charging of li-ion cells: part ii. nonlinear contributions to cell and electrode polarization. J. Electrochem. Soc. *166*, A3305–A3313.

17. Verbrugge, M.W., and Koch, B.J. (1997). The effect of large negative potentials and overcharge on the electrochemical performance of lithiated carbon. J. Electroanal. Chem. *436*, 1–7.

18. Wandt, J., Jakes, P., Granwehr, J., Eichel, R.-A., and Gasteiger, H.A. (2018). Quantitative and time-resolved detection of lithium plating on graphite anodes in lithium ion batteries. Mater. Today *21*, 231–240.

19. Bai, P., Li, J., Brushett, F.R., and Bazant, M.Z. (2016). Transition of lithium growth mechanisms in liquid electrolytes. Energy Environ. Sci. *9*, 3221–3229.

20. Legrand, N., Knosp, B., Desprez, P., Lapicque, F., and Raël, S. (2014). Physical characterization of the charging process of a li-ion battery and prediction of li plating by electrochemical modelling. J. Power Sources *245*, 208–216.

21. Sand, H.J.S. (1901). III. On the concentration at the electrodes in a solution, with special reference to the liberation of hydrogen by electrolysis of a mixture of copper sulphate and sulphuric acid. Lond. Edinb. Dublin Philos. Mag. J. Sci. *1*, 45–79.

22. Dydek, E.V., Zaltzman, B., Rubinstein, I., Deng, D.S., Mani, A., and Bazant, M.Z. (2011). Overlimiting current in a microchannel. Phys. Rev. Lett. *107*, 118301.

23. Cannarella, J., and Arnold, C.B. (2015). The effects of defects on localized plating in lithium-ion batteries. J. Electrochem. Soc. *162*, A1365–A1373.

24. Grier, D., Ben-Jacob, E., Clarke, R., and Sander, L.M. (1986). Morphology and microstructure in electrochemical deposition of zinc. Phys. Rev. Lett. *56*, 1264–1267.

25. Léger, C., Elezgaray, J., and Argoul, F. (1998). Dynamical characterization of one-dimensional stationary growth regimes in diffusion-limited electrodeposition processes. Phys. Rev. E *58*, 7700–7709.

26. Fraggedakis, D., Nadkarni, N., Gao, T., Zhou, T., Zhang, Y., Han, Y., Stephens, R.M., Shao-Horn, Y., and Bazant, M.Z. (2020b). A scaling law to determine phase morphologies during ion intercalation. Energy Environ. Sci. *13*, 2142–2152.

27. Smith, R.B., Khoo, E., and Bazant, M.Z. (2017). Intercalation kinetics in multiphase-layered materials. J. Phys. Chem. C *121*, 12505–12523.

28. Bazant, M.Z. (2013). Theory of chemical kinetics and charge transfer based on nonequilibrium thermodynamics. Acc. Chem. Res. *46*, 1144–1160.

29. Bazant, M.Z. (2017). Thermodynamic stability of driven open systems and control of phase separation by electro-autocatalysis. Faraday Discuss. *199*, 423–463.

30. Harris, S.J., Timmons, A., Baker, D.R., and Monroe, C. (2010). Direct in situ measurements of li transport in li-ion battery negative electrodes. Chem. Phys. Lett. *485*, 265–274.

31. Tang, M., Albertus, P., and Newman, J. (2009). Two-dimensional modeling of lithium deposition during cell charging. J. Electrochem. Soc. *156*, A390.

32. Tanim, T.R., Paul, P.P., Thampy, V., Cao, C., Steinrück, H.-G., Nelson Weker, J.N., Toney, M.F., Dufek, E.J., Evans, M.C., Jansen, A.N., et al. (2020). Heterogeneous behavior of lithium plating during extreme fast charging. Cell. Rep. Phys. Sci. *1*, 100114.

33. Yao, K.P.C., Okasinski, J.S., Kalaga, K., Shkrob, I.A., and Abraham, D.P. (2019). Quantifying lithium concentration gradients in the graphite electrode of li-ion cells using operando energy dispersive x-ray diffraction. Energy Environ. Sci. *12*, 656–665.

34. Thomas-Alyea, K.E., Jung, C., Smith, R.B., and Bazant, M.Z. (2017). In situ observation and mathematical modeling of lithium distribution within graphite. J. Electrochem. Soc. *164*, E3063–E3072.

35. Colclasure, A.M., Tanim, T.R., Jansen, A.N., Trask, S.E., Dunlop, A.R., Polzin, B.J., Bloom, I., Robertson, D., Flores, L., Evans, M., et al. (2020). Electrode scale and electrolyte transport effects on extreme fast charging of lithium-ion cells. Electrochim. Acta *337*, 135854.

36. Gallagher, K.G., Dees, D.W., Jansen, A.N., Abraham, D.P., and Kang, S.-H. (2012). A volume averaged approach to the numerical modeling of phase-transition intercalation electrodes presented for lixc6. J. Electrochem. Soc. *159*, A2029–A2037.

37. Mistry, A., Usseglio-Viretta, F.L.E., Colclasure, A., Smith, K., and Mukherjee, P.P. (2019). Fingerprinting redox heterogeneity in electrodes during extreme fast charging. J. Electrochem. Soc. *167*.

38. Li, N., Zhang, K., Xie, K., Wei, W., Gao, Y., Bai, M., Gao, Y., Hou, Q., Shen, C., Xia, Z., and Wei, B. (2020). Reduced-graphene-oxide-guided directional growth of planar lithium layers. Adv. Mater. *32*, e1907079.

39. Sun, Y., Zheng, G., Seh, Z.W., Liu, N., Wang, S., Sun, J., Lee, H.R., and Cui, Y. (2016). Graphite-encapsulated li-metal hybrid anodes for high-capacity li batteries. Chem *1*, 287–297.

40. Yang, X.-G., Leng, Y., Zhang, G., Ge, S., and Wang, C.-Y. (2017). Modeling of lithium plating induced aging of lithium-ion batteries: transition from linear to nonlinear aging. J. Power Sources *360*, 28–40.

41. Ferguson, T.R., and Bazant, M.Z. (2012). Nonequilibrium thermodynamics of porous electrodes. J. Electrochem. Soc. *159*, A1967–A1985.

42. Ferguson, T.R., and Bazant, M.Z. (2014). Phase transformation dynamics in porous battery electrodes. Electrochim. Acta *146*, 89–97.

43. Smith, R.B., and Bazant, M.Z. (2017). Multiphase porous electrode theory. J. Electrochem. Soc. *164*, E3291–E3310.

44. Monroe, C., and Newman, J. (2003). Dendrite growth in lithium/polymer systems. J. Electrochem. Soc. *150*, A1377–A1384.

45. Fraggedakis, D., and Bazant, M.Z. (2020). Tuning the stability of electrochemical interfaces by electron transfer reactions. J. Chem. Phys. *152*, 184703.

46. Fraggedakis, D., McEldrew, M., Smith, R.B., Krishnan, Y., Zhang, Y., Chueh, W., Bai, P., Shao-Horn, Y., and Bazant, M.Z. (2020a). Theory of coupled ion-electron transfer kinetics. Electrochimica Acta. https://doi.org/10.1016/j.electacta.2020.137432.

47. Chen, X., Chen, X.R., Hou, T.Z., Li, B.Q., Cheng, X.B., Zhang, R., and Zhang, Q. (2019). Lithiophilicity chemistry of heteroatom-doped carbon to guide uniform lithium nucleation in lithium metal anodes. Sci. Adv. *5*, eaau7728.

48. Zhang, R., Chen, X.-R., Chen, X., Cheng, X.-B., Zhang, X.-Q., Yan, C., and Zhang, Q. (2017). Lithiophilic sites in doped graphene guide uniform lithium nucleation for dendrite-free lithium metal anodes. Angew. Chem. Int. Ed. Engl. *56*, 7764–7768.

49. Dahn, J.R. (1991). Phase diagram of li x c 6. Phys. Rev. B *44*, 9170–9177.

50. Schweidler, S., de Biasi, L., Schiele, A., Hartmann, P., Brezesinski, T., and Janek, J. (2018). Volume changes of graphite anodes revisited: a combined operando x-ray diffraction and in situ pressure analysis study. J. Phys. Chem. C *122*, 8829–8835.

51. Funabiki, A., Inaba, M., and Ogumi, Z. (1997). A.c. impedance analysis of electrochemical lithium intercalation into highly oriented pyrolytic graphite. J. Power Sources *68*, 227–231.

52. Persson, K., Hinuma, Y., Meng, Y.S., Van der Ven, A., and Ceder, G. (2010). Thermodynamic and kinetic properties of the li-graphite system from first-principles calculations. Phys. Rev. B *82*, 125416.

53. Chen, Y., Wang, Z., Li, X., Yao, X., Wang, C., Li, Y., Xue, W., Yu, D., Kim, S.Y., Yang, F., et al. (2020). Li metal deposition and stripping in a solid-state battery via coble creep. Nature *578*, 251–255.

54. Kushima, A., So, K.P., Su, C., Bai, P., Kuriyama, N., Maebashi, T., Fujiwara, Y., Bazant, M.Z., and Li, J. (2017). Liquid cell transmission electron microscopy observation of lithium metal growth and dissolution: root growth, dead lithium and lithium flotsams. Nano Energy *32*, 271–279.

55. Gamburg, Y.D., and Zangari, G. (2011). Theory and Practice of Metal Electrodeposition (Springer Science & Business Media).

56. Popov, K., Grgur, B., and Djokić, S.S. (2007). Fundamental Aspects of Electrometallurgy (Springer).

57. Zinth, V., von Lüders, C., Hofmann, M., Hattendorff, J., Buchberger, I., Erhard, S., Rebelo-Kornmeier, J., Jossen, A., and Gilles, R. (2014). Lithium plating in lithium-ion batteries at sub-ambient temperatures investigated by in situ neutron diffraction. J. Power Sources *271*, 152–159.

58. Lai, S.C., Patel, A.N., McKelvey, K., and Unwin, P.R. (2012). Definitive evidence for fast electron transfer at pristine basal plane graphite from high-resolution electrochemical imaging. Angew Chem Int Ed Engl *51*, 5405–5408.

59. Zhang, G., Kirkman, P.M., Patel, A.N., Cuharuc, A.S., McKelvey, K., and Unwin, P.R. (2014). Molecular functionalization of graphite surfaces: basal plane versus step edge electrochemical activity. J. Am. Chem. Soc. *136*, 11444–11451.

60. Duan, J., Zheng, Y., Luo, W., Wu, W., Wang, T., Xie, Y., Li, S., Li, J., and Huang, Y. (2020). Is graphite lithiophobic or lithiophilic? Natl. Sci. Rev. *7*, 1208–1217.

61. Nadkarni, N., Zhou, T., Fraggedakis, D., Gao, T., and Bazant, M.Z. (2019). Modeling the metal–insulator phase transition in lixcoo2 for energy and information storage. Adv. Funct. Mater. *29*, 1902821.

62. Bai, P., and Bazant, M.Z. (2014). Charge transfer kinetics at the solid–solid interface in porous electrodes. Nat. Commun. *5*, 3585.

63. Zeng, Y., Smith, R.B., Bai, P., and Bazant, M.Z. (2014). Simple formula for Marcus–Hush–Chidsey kinetics. J. Electroanal. Chem. *735*, 77–83.

64. Bai, P., Guo, J., Wang, M., Kushima, A., Su, L., Li, J., Brushett, F.R., and Bazant, M.Z. (2018). Interactions between lithium growths and nanoporous ceramic separators. Joule *2*, 2434–2449.

65. Ely, D.R., and García, R.E. (2013). Heterogeneous nucleation and growth of lithium electrodeposits on negative electrodes. J. Electrochem. Soc. *160*, A662–A668.

66. Fraggedakis, D., Papaioannou, J., Dimakopoulos, Y., and Tsamopoulos, J. (2017). Discretization of three-dimensional free surface flows and moving boundary problems via elliptic grid methods based on variational principles. J. Comp. Phys. *344*, 127–150.

67. Yamaki, J.-i., Tobishima, S.-i., Hayashi, K., Keiichi Saito, K., Nemoto, Y., and Arakawa, M. (1998). A consideration of the morphology of electrochemically deposited lithium in an organic electrolyte. J. Power Sources *74*, 219–227.

68. Aogaki, R., and Makino, T. (1981). Theory of powdered metal formation in electrochemistry—morphological instability in galvanostatic crystal growth under diffusion control. Electrochim. Acta *26*, 1509–1517.

69. Heß, M., and Novák, P. (2013). Shrinking annuli mechanism and stage-dependent rate capability of thin-layer graphite electrodes for lithium-ion batteries. Electrochim. Acta *106*, 149–158.

70. Gallagher, K.G., Trask, S.E., Bauer, C., Woehrle, T., Lux, S.F., Tschech, M., Lamp, P., Polzin, B.J., Ha, S., Long, B., et al. (2016). Optimizing areal capacities through understanding the limitations of lithium-ion electrodes. J. Electrochem. Soc. *163*, A138–A149.

71. Yang, X.G., Zhang, G., Ge, S., and Wang, C.Y. (2018). Fast charging of lithium-ion batteries at all temperatures. Proc. Natl. Acad. Sci. USA *115*, 7266–7271.

72. Sieg, J., Bandlow, J., Mitsch, T., Dragicevic, D., Materna, T., Spier, B., Witzenhausen, H., Ecker, M., and Sauer, D.U. (2019). Fast charging of an electric vehicle lithium-ion battery at the limit of the lithium deposition process. J. Power Sources *427*, 260–270.

73. Konz, Z.M., McShane, E.J., and McCloskey, B.D. (2020). Detecting the onset of lithium plating and monitoring fast charging performance with voltage relaxation. ACS Energy Lett *5*, 1750–1757.

74. Petzl, M., and Danzer, M.A. (2014). Nondestructive detection, characterization, and quantification of lithium plating in commercial lithium-ion batteries. J. Power Sources *254*, 80–87.

JOUL, Volume *5*

Supplemental Information

Interplay of Lithium Intercalation and Plating on a Single Graphite Particle

Tao Gao, Yu Han, Dimitrios Fraggedakis, Supratim Das, Tingtao Zhou, Che-Ning Yeh, Shengming Xu, William C. Chueh, Ju Li, and Martin Z. Bazant

CHEMICAL POTENTIAL AND VOLTAGE

To better understand the experiment results, especially to relate the observed voltage-capacity curve with the intercalation and phase transition of graphite as well as Li plating (Fig.S12), we derive the equation to relate observed voltage with chemical potential using chemical kinetics based on non-equilibrium thermodynamics.[1]

In this experiment, the intercalation reaction happening at the working electrode (HOPG particle) and the redox reaction at the reference electrode (Li metal) can be written respectively as:

$$Li^+ + e^- + M \iff LiM \tag{S1}$$

$$Li^+ + e^- \iff Li \tag{S2}$$

At the working electrode, Li^+ intercalates into the host structure of graphite, consumes one electron, occupies one interstitial site from the host (M) and generates one Li-e polaron (LiM). At the reference electrode, Li^+ is reduced by one electron and deposits as Li atom.

The affinity A, which is the difference in chemical potential between the products and reactants, equals $e\eta$ and measures the driving force of the reaction. The affinity for each reaction S1 and S2 are

$$A_w \equiv e\eta_w = \mu_{LiM} - \mu_M - (\mu_{Li^+,w} + e\phi_{l,w} - e\phi_{s,w}) = \mu_s - (\mu_{Li^+,w} + e\phi_{l,w} - e\phi_{s,w}) \tag{S3}$$

$$A_r \equiv e\eta_r = \mu_{Li} - (\mu_{Li^+,r} + e\phi_{l,r} - e\phi_{s,r}) \tag{S4}$$

in which subscripts l, s, w, r refer to liquid phase (electrolyte), solid phase (electrode), working electrode and reference electrode, respectively. ϕ is electrostatic potential. μ is the chemical potential of each species in the reaction. μ_s is the diffusional chemical potential at the graphite edge surface, which measures the energy change when a vacancy in the host (M) is replaced by a polaron (LiM). η_w and η_r are the overpotential for the reactions at working and reference electrode.

The half cell potentials $\Delta\phi$, defined as $\phi_s - \phi_l$ for each electrode, are

$$\Delta\phi_w = -\frac{\mu_s}{e} + \frac{\mu_{Li^+,w}}{e} + \eta_w \tag{S5}$$

$$\Delta\phi_r = -\frac{\mu_{Li}}{e} + \frac{\mu_{Li^+,r}}{e} + \eta_r \tag{S6}$$

The measured voltage in the experiment is the difference in the electrostatic potential between the working and reference

$$V = \phi_w - \phi_r = \Delta\phi_w - \Delta\phi_r + (\phi_{l,w} - \phi_{l,r}) = -\frac{\mu_s - \mu_{Li}}{e} + \frac{\mu_{Li^+,w} - \mu_{Li^+,r}}{e} + (\eta_w - \eta_r) + (\phi_{l,w} - \phi_{l,r}) \tag{S7}$$

The equation can be greatly simplified at equilibrium. At equilibrium, there is no reaction so overpotential is zero. There is no gradient in the electrolyte electrostatic potential or chemical potential of Li^+ leading to $\mu_{Li^+,w} \simeq \mu_{Li^+,r}$ and $\phi_{l,w} \simeq \phi_{l,r}$. Using the chemical potential of Li metal as the reference for chemical potential, the measured voltage is

$$V = -\frac{\mu_s}{e} \tag{S8}$$

which suggests that the open circuit voltage of the battery directly reflects the diffusional chemical potential of graphite.

In a typical experiment, the applied current, 50 μA, corresponds to a current density of 1.25 mA/cm^2, which is much smaller than the diffusion limiting current $J_{lim} = 2c_0FD/(t_aL) \approx$ 32 mA/cm^2 for a particle thickness of 100 μm and separator thickness of 10 μm. Therefore, the gradient in the electrolyte electrostatic and chemical potential of Li^+ are negligible. In addition, the reaction on the reference electrode is facile so $\eta_r \approx 0$. We have

$$V \approx -\frac{\mu_s}{e} + \eta_w \tag{S9}$$

CHEMICAL POTENTIAL AND PHASE TRANSITION

The diffusional chemical potential as a function of local concentration is given in Fig. S13. The vertical dash line shows the binodal region. Once the local concentration enters the binodal region and crosses spinodal point, phase separation happens. During lithiation, the surface concentration of HOPG increases, and the blue-red phase transition is triggered once c_s is over 0.2, which means the c_s will jump to 0.5 once the red phase forms. After that, c_s will continue to increase, and the red-gold phase transition will be triggered once c_s enters the second spinodal region.

BLACK FLOC-LIKE MATTER FORMED DURING LI DISSOLUTION

We hypothesize this is micron-sized lithium covered by nanometer thick solid electrolyte interface (SEI). Bulky lithium metal shows a silver color. The color transforms to black, however,

when the particle size reduces into micron regime. This happens because the dissolution reaction is intrinsically a corrosion reaction. During the transition of bulky lithium to stacking of micron-particles of lithium, it loses both the shining color. Once all bulk lithium has been transformed into micron-particles, the percolating pathway for electrons is lost since the particles are separated by the surface film, which is highly ionic conductive but electronic insulating. Therefore, oxidation of these small particles becomes kinetically difficult (happening at plateau of 400 mV).

CURRENT DENSITY ON GRAPHITE PARTICLES IN COMMERCIAL BATTERIES

We use the current density at the edge surface of the graphite particle to characterize the lithiation rate and make comparison between our study with the commercial graphite electrode under fast charging condition. Current density at the edge surface is a better parameter than C-rate to characterize the dynamics of graphite for the following reason. Graphite has a layered structure in which Li primarily diffuse between the layers and insertion reaction primarily happens at the edge plane of graphite. Current density at the edge surface is a reaction area averaged lithiation rate, which appropriately accounts for the reaction rate at the active crystal plane and the resulted anisotropic lithiation dynamics. In contrast, C-rate is a volume averaged quantity, which neglects the effect of such anisotropy.

For a typical HOPG particle operating at 10-100 μA in this study, the lithiation rate is 1.25-12.5 mA/cm^2 at the edge surface. For commercial graphite electrode with graphite flake and mass loading of 1.5-5 mA/cm^2, the 10 min charging corresponds to a lithiation rate of 0.83-15.1 mA/cm^2. Therefore, the chosen experimental condition in our study can reflect the local particle scale dynamics of commercial graphite electrode under fast charging condition. The details of the calculation are given below.

A typical commercial graphite electrode using graphite flake has a particle size (D50) of 3.3 um and thickness of 0.4 μm.[2] For such a particle, 10 min (6C) charging rate corresponds to 0.83 mA/cm^2 at the edge surface. Since the sizes of the particles are not uniform in real battery electrode, the size effect needs to be considered when evaluating the current density at individual particles. Assuming all the particles have the same geometry (cylinder shape and fixed R/h ratio), the capacity scales with R^3, and edge surface area scales with R^2, therefore current density at the edge surface scales with R. For this reason, larger particles experience higher current density at their edge surface. For the same electrode in reference[2], the D90 is 6 μm. At this size, 10 min (6C) charging rate corresponds to 1.51 mA/cm^2 at the edge surface.

The above discussion assumes the same charging time for all particles in the porous electrode. In practice, however, this assumption does not hold. Reaction heterogeneity among the constituent particles are observed in both experiment and simulation.[3–5] For thick electrode, the lithiation rate on the particles near separator can be 2-10 times higher than the homogeneously averaged lithiation rate.[5, 6] Considering this heterogeneity, the actual lithiation rate on a graphite particle in a real commercial graphite electrode falls in the range of 0.83-15.1 mA/cm^2.

THE SOURCE OF LI FOR THE PLATED PHASE

The source of Li for the plated phase is still under debate. In pure metallic substrate, such as Cu [7], it is clear that the Li reservoir is the electrolyte itself. However, when plating occurs on an intercalation material, such as graphite, then a second 'source' of Li might be considered. In particular, we can think of the intercalated Li to be converted into plated Li. In order to understand if this is the case, we need to resort to a picture which involves the electrostatics at the graphite/Plated Li contact.

In general, it is well known that the metallic Li has lower work function than C_6 and LiC_6. This can be translated in terms of the Fermi level of each material, i.e. C_6 and LiC_6 have lower Fermi energy than Li metal [8]. Therefore, when we put in contact the two materials, electrons are going to flow from the material with high electronic energy to the low one (from Li metal to graphite). Because of the metallic nature of both Li metal and Li_xC_6, surface charges will build up on the two interfaces. More specifically, Li metal and C_6/LiC_6 will have positive and negative charges, respectively. Additionally, an electric field $\mathbf{E}$ will build up on the contact between the two different phases, which will point towards the graphite, Fig. S15. To first order approximation, one can consider the electrostatic force on the holes ('bare' Li ions) to be $\mathbf{F} = q\mathbf{E}$, so the surface Li ions would like to be detached from the plated Li and enter the graphite. Moreover, Li exists inside graphite as an ion [8], and thus there is an attractive force between the Li^+-e^- pairs inside graphite. According to this physical picture, it is highly unlikely for the intercalated Li to want to leave its host material, C_6. To this end, using these first order assumptions, we conclude that the major Li source for the plated Li is electrolyte.

MATHEMATICAL MODEL

The model system is a layered sandwich of a lithium reference electrode, electrolyte layer, plated lithium (after it starts growing) and active particle graphite, in that order from left to right. We define all potentials with respect to the equilibrium potential of Li/Li^+. The electrolyte layer in contact with the reference lithium electrode is considered to be an infinite reservoir of lithium ions. Current applied during the charging (lithiation of graphite) step is assumed positive as a convention. Kinetics for intercalation is described using a formulation for concerted transfer of ions and electrons in non-equilibrium conditions. Kinetics of the side reaction (lithium plating) is described using a Butler-Volmer formulation with a pre-factor that scales with the volume of lithium deposited per unit area. Lithiated graphite is known to spontaneously phase separate at certain concentrations in the free-energy landscape which gives rise to the 'staging' behavior. Multi-variable frameworks accounting for two/three layer interactions of ions can mostly describe lithium intercalation at high-filling fractions, but it cannot easily describe the plethora of stable or metastable phases in graphite at low-filling fractions (not only for lithium), which exhibit longer range periodicity across three or more layers. To capture this staging, we use a single-variable free-energy model for lithium intercalation in graphite, developed by Alyea et al. [4]. The expression is fitted to the open circuit voltage at low filling fractions as an effective solid solution, while still captures the two primary voltage plateaus at high filling fractions. The free energy permits construction of two common tangents between filling fractions near 0.3 and 0.5 and another between filling fractions near 0.5 and 0.9 which leads to the two clear voltage plateaus and two sharp moving fronts.

Validation: Validation of a 1D model using experimental data on a mm scale graphite particle involves a few steps to simplify the experimental system being studied. We assume isotropic solid diffusivity, and extract a small vertical slice (around 50x500 pixels in dimension) from the top left of the particle (shown in Red dotted lines in Figure 2b on Particle A in main text). The jagged edge slope of the HOPG particle is removed digitally to prevent erroneous readings from image processing. The final snipped image is contrast-enhanced and then processed using an algorithm, assisted by the MATLAB Image Processing Toolbox, to convert the observed colors on graphite to a time-dependent solid-phase concentration map. The image processing does not change the signature of the colors in any way. This concentration profile used to compare theoretical predictions of the time evolution of plated lithium volume from the model. Parameters in the theory are obtained from fitting to the lithiation voltage curve from multiple repeats of the experiment.

Thermodynamics: The expression for μ_h is taken from Appendix A of Ref [4]. The non-homogeneous chemical potential can be obtained by taking the derivative of the gradient energy penalty term, following Cahn and Hilliard [9], $\mu_{nh} = -\kappa\nabla^2 c$. Combining these two expressions we get,

$$\mu = \frac{\delta G}{\delta c} = \mu_h - \kappa\nabla^2 c \tag{S10}$$

Diffusivity: Persson et al. [10] studied the energetics of stage I and stage II graphite intercalation compounds using a generalized gradient approximation (GGA) to density functional theory (DFT), and employed Kinetic Monte-Carlo simulations to calculate lithium diffusion coefficients as a function of lithium concentration. Since stages I and II dominate the lithium-graphite phase diagram, we directly use the results given in log-linear plot in Figure 3 in Ref. [10] to describe D as a function of $\tilde{c}$ (scaled to the electrolyte concentration c_{max}) using a straight line. The best fit linear relations obtained from the data are:

$$log_{10}\left(D\ [cm^2/s]\right) = \begin{cases} -5.55\ \tilde{c} - 6.69 \ \text{ if } \tilde{c} \leq 0.5\ (stage\ II) \\ -2.21\ \tilde{c} - 7.15 \ \text{ if } \tilde{c} > 0.5\ (stage\ I) \end{cases} \tag{S11}$$

Concentration Boundary Conditions: The conservation of Li conservation admits the following boundary conditions: 1) $\hat{\boldsymbol{n}} \cdot (\kappa\nabla c)_s = \frac{\partial \gamma_s}{\partial c}$, where γ_s is the surface energy and $\hat{\boldsymbol{n}}$ is an outward facing unit normal vector. Although surface "wetting" has been shown to be important in nanoparticle dynamics [11], we set $\hat{\boldsymbol{n}}(\kappa\nabla c)_s = 0$ here. 2) The galvanostatic boundary condition $\frac{i}{e} = -\hat{\boldsymbol{n}} \cdot \boldsymbol{j}$.

Lithium plating: The electrochemical reaction associated with lithium plating is given by:

$$Li^+ + e^- \rightleftharpoons Li^0$$

The reaction can be described by symmetric (i.e. $\alpha = 0.5$) Butler-Volmer formulations. Herein we define two separate plating current densities: $i_{pl,m}$ based on the actual microscopic surface area of the edge plane being plated with Li (A_{Li}), varying with time as lithium nuclei grow/coalesce, and i_{pl} based on the projected area of the plated lithium nuclei onto the edge plane of the HOPG particle (A_p). Both current densities can be written as,

$$i_{pl,m} = i_{0,pl,m}\left[\exp(-\alpha\tilde{\eta}_{pl}) - \exp\left((1-\alpha)\tilde{\eta}_{pl}\right)\right] \tag{S12}$$

$$i_{pl} = i_{0,pl}\left[\exp(-\alpha\tilde{\eta}_{pl}) - \exp\left((1-\alpha)\tilde{\eta}_{pl}\right)\right] \tag{S13}$$

where we neglect the surface energy contribution to the overpotential in the microscopic reaction model [12] for simplicity, since the geometry is also changing rapidly and not known to have a certain shape, such as a hemisphere. Since both these expressions describe the same physical phenomena and must conserve charge, they are related as,

$$A_{Li} i_{pl,m} = A_p i_{pl} \implies A_{Li} i_{0,pl,m} = A_p i_{0,pl} \tag{S14}$$

The rate of lithium growth depends on the exposed microscopic surface area (A_{Li}) of deposited mossy lithium. As lithium nuclei grow, the ratio of the microscopic surface area to the projected area increases with time. By the law of conservation of charge, we equate the sum of the intercalation and plating currents to the applied current i as,

$$i A_{edge} = i_{int} A_{edge} + i_{pl} A_p \tag{S15}$$

The projected area of plated Li nuclei at the time of onset is assumed to be 1% of the left edge plane area A_{edge} of the HOPG particle, i.e. $A_p = 0.01 \times A_{edge}$. From the experimental videos, it can be visually estimated that the first observable lithium nuclei cluster growth occupies about 10% of the left edge length of the particle. Extending the same scaling to the depth dimension of the left edge plane as well, we estimate that the actual projected area of Li growth at onset is 1% of the left edge plane area of 0.1 mm^2.

The plating current contributes to the growth of deposited/plated lithium volume V_{Li} as:

$$\frac{1}{\Omega}\frac{dV_{Li}}{dt} = A_{Li}\frac{i_{pl,m}}{e} = A_p \frac{i_{pl}}{e} \tag{S16}$$

Here, we define $A_{Li} = A_{nuc}\left(\frac{V_{Li}}{V_{nuc}}\right)^{\beta}$. The choice $\beta = 2/3$ would describe normal non-fractal growth ($A \sim L^2$ and $V \sim L^3$ so $A \sim V^{2/3}$), including the prototypical case of a hemispherical nucleus. Over time, the exponent may decrease as nuclei merge into a film of nearly constant area ($\beta = 0$), or increase after highly ramified fractal dendrites form ($2/3 < \beta < 1$). Ω is the molar volume of lithium [13], and A_{nuc} and V_{nuc} are the total microscopic surface area and volume of the deposited lithium nuclei, which scales with the total number of nuclei N as, $A_{nuc} = A_{0,nuc} \times N$ and $V_{nuc} = V_{0,nuc} \times N$. $A_{0,nuc}$ and $V_{0,nuc}$ are the microscopic surface area and volume of a single lithium nucleus of critical radius that will spontaneously grow under the influence of current. The thermodynamic stability of a nucleus that deposits on an electrically charged substrate is determined by the bulk free energy of transformation, both chemical and electrical, and the surface tension contributions. For a single, isolated, hemispherical electrodeposit, the kinetic critical radius corresponding to the case where

the Laplace pressure balances the applied overpotential, is given by [13],

$$r^*_{nuc} = \frac{2\gamma\Omega}{zF\eta_{pl}} \tag{S17}$$

For an observed plating onset overpotential $\eta_{pl} \sim 0.15$ V vs. Li/Li^+ in our experiments (see Fig 5 in the main text), the kinetic critical radius r^*_{nuc} is approximately 0.75 nm. $A_{0,nuc}$ and $V_{0,nuc}$ for a growing hemisphere at critical radius subsequently can be calculated using $A_{0,nuc} = 2\pi {r^*_{nuc}}^2$ and $V_{0,nuc} = (2/3)\pi {r^*_{nuc}}^3$.

During growth of the mossy Li deposits, lithium nuclei merge into larger ones, leading to a transient variation of the total number of nuclei present in the system. However, since we are focused on the time regime of onset of plating, it is reasonable to assume that the number of nuclei N remains roughly constant in this period. The resolution of the experimental data is also insufficient to reliably extract information about nucleation and growth statistics, so we choose to forego the inclusion of a time dependent N whose distribution could be described using a Johnson-Mehl-Avrami-Kolmogorov (JMAK) modeling framework [14–16], in favor of a simpler model. We start with a monolayer coverage of lithium nuclei at kinetic critical radius covering the plating area A_p. So the total number of nuclei $N = A_p/A_{0,nuc} \sim 5.7 \times 10^8$. We note that N is a very large number, and the initial nuclei are far too small to be experimentally observed with an optical microscope. The resulting model should serve our purposes of accurately describing the onset of lithium plating on graphite, although not the long-time growth of significant mossy or dendritic deposits.

Additionally, by Equation S15 we assume that $i_{pl} \sim constant$ since $i_{int} \to 0$ after plating onset (see Figure 6D inset in main text). To obtain a time dependence of the plating exchange current and to verify the validity of the $i_{pl} \sim constant$ assumption, we perform a scaling analysis on Equation S16 which reveals a scaling of V_{Li} with time t as,

$$V_{Li} \approx \frac{A_p i_{pl} \Omega}{e}\, t \tag{S18}$$

Substituting this scaling into the relation for $i_{0,pl,m}$ and $i_{0,pl}$ in Equation S14, we get,

$$i_{0,pl,m} = i_{0,pl} \frac{A_p}{A_{nuc}} \left(\frac{eV_{nuc}}{A_p i_{pl} \Omega t_0} \right)^{\beta} \tilde{t}^{-\beta} \tag{S19}$$

The first two groups of variables in Equation S19 are known constants. t is non-dimensionalized by t_0, the time at which lithium nuclei surpass the critical radius r^*_{nuc}, at 3120s from the start of the experiment. Direct nanoscale observations of hemispherical lithium growth on a gold electrode by Kushima et al. [17] revealed that the size of the hemisphere grew roughly as the square root

of time (i.e. $R \sim t^{1/2}$) , which was quantitatively attributed to SEI growth on the deposited lithium. If the same mechanism were at work here, a microscopic exchange current density in 3D of $i_{0,pl,m} \propto t^{-1/2}$ would imply $\beta = 1/2$. Substituting back into Equation S16 with $\beta = 2/3$ for the hemispherical geometry, however, would yield a scaling $i_{pl} \propto t^{-1/2}t^{2/3} = t^{1/6}$, which is slowly varying and seemingly consistent with the original assumption that $i_{pl} \sim$ constant.

On the other hand, there are good reasons to expect additional mechanisms to slow down the microscopic plating reaction, which make the approximation of constant projected exchange current very reasonable, at least for the early stages of nucleation and growth of lithium metal. (1) The geometrical exponent β controlling the surface to volume ratio must slowly decrease from 2/3 (for separate hemispherical nuclei) as nuclei merge and coalesce and could decrease of even surpass $\beta = 1/2$ (for constant growth per projected area) since $\beta = 0$ is the value for dense flat film. (2) The number of nuclei will also decrease, as they merge to form a continuous deposit, and $N \sim t^{-1/2}$ could also justify the same result, with $\beta = 2/3$. (3) The microscopic overpotential has an additional contribution for curvature, which scales with inverse radius and decays with time as the initial nanoscale nuclei grow and merge into a film covering the surface. For all of these reasons, the detailed microscopic growth is quite complicated and yet consistent with the simple assumption of nearly constant macroscopic exchange current density $i_{0,pl}$ per projected area of lithium growth.

As plotted in Figure 5f in the main text, the voltage of the cell reaches a minimum value subsequent to which mossy lithium starts to deposit on the edge of the graphite particle. We propose that the offset of the voltage curve minimum from the 0 V line is the barrier for the first lithium nucleus to surpass the kinetic critical radius. The voltage barrier could have several physical origins - it could be influenced by the surface tension γ of lithium/electrolyte as the nucleus reaches the critical volume (see section: *Derivation of plating exchange current and degree of certainty*). It could also be the energy required for nucleation in the presence of a solid-electrolyte interphase (SEI) layer on the graphite active surface, in which case the critical voltage and critical radius might be a function of the cycling history of the cell. SEI also grows rapidly on fresh lithium nuclei [17] and thus the overpotential required for continued growth may deviate from that predicted by the classical nucleation theory framework presented in this paper.

Subsequent to spontaneous lithium nuclei growth on the edge-plane of graphite, the energy barrier for lithium growth becomes significantly smaller as the lithium wets the LiC_6 surface and the lack of vacant sites at graphite surface makes Li intercalation kinetically difficult. We define a barrier potential V_n, dependent on the volume of lithium deposited (V_{Li}) based on a Gaussian

function as,

$$V_n = V_{0,n} e^{-V_{Li}^2/2V_{nuc}^2} \tag{S20}$$

$V_{0,n}$ is assumed to be approximately 0.15 V from the experimental observations in Figure 5 in the main text. The exponential term ensures that the barrier potential goes to zero as the lithium content increases on the surface. The nucleation barrier affects the overpotential of the lithium plating reaction by lowering the equilibrium potential from 0 V as, $\eta_{pl} = \Delta\phi - (0 - V_n)$.

Numerical Methods: The domain is discretized in 1D with the left boundary as the graphite/electrolyte interface and the right boundary as a point inside the bulk of the HOPG particle where the bottom edge of the image slice is. The size of the slice is chosen such that the domain never becomes 'full' with lithium. This ensures that the simulation is always able to capture the interplay of bulk diffusion and surface intercalation at all time points in the experiment. The potential field $\phi(t)$ is assumed uniform in space as graphite is a good conductor of electrons, and only solved for in the time domain. The intercalated lithium concentration $c(x,t)$ is solved for evolution in space and time. The fourth-order Cahn-Hilliard equation (Eq. 2 in main text), the plated lithium growth equation S16, the barrier potential equation S20 and the constant current constraint equation S15 in the Equations section are solved as a system of differential algebraic equations (DAE). We take the general approach of discretizing each in space using some variant of the finite volume method to obtain the system of DAEs, and then stepping in time using a variable-order adaptive time stepper, ODE15s in MATLAB. We discretize in space using finite volume methods both for their robustness to steep gradients and also their mass conservation to within numerical accuracy. The width of a finite volume is chosen such that it is smaller than the interfacial width $\left(\lambda_b \sim \sqrt{\frac{\kappa}{c_{ref}\Omega_b}}\right)$ following Refs. [18] and [19]. The values of κ, c_{ref} and Ω_b of graphite are taken from Ref. [18]. The ODE15s function, based on a variant of the backward differentiation formula, handles the formation of all underlying system matrices and interactions with other numerical libraries involved in the time integration.

Some Additional Results: Our simulations demonstrate the predictability of the phase field model for graphite as it can qualitatively capture the observed Li ion concentration evolution in the particle. Additionally, Fig. 6D in the main text demonstrates the fitted and experimentally observed voltage vs. charge profiles. Fig. 6E in the main text depicts the the model predictions on the voltage V and surface concentration c_s under delithiation.

The model can predict the onset of Li plating and the correct value of the nucleation voltage. As discussed in Fig. 5 based on the experimental observations, Li plating occurs only when the surface of graphite becomes saturated by the inserted Li ions. Fig. S16 demonstrates the evolution of the surface concentration as a function of the average Li fraction in the graphite particle. Our calculations show that when the surface concentration c_s becomes 1 the nucleation barrier is exceeded. Furthermore, a solid solution model (Figure S16 e-h) is insufficient in its ability to predict the onset of lithium plating correctly. Fig. S17 depicts the predicted rest and delithiation profiles, corresponding to the potential curves shown in Fig 6E in the main text. Upon comparison with experimental results in Figure 4 in the main text, one can conclude that the model, fitted only to lithiation voltage profiles, can predict the system behavior during rest and delithiation reasonably well. During rest, some of the plated Li dissolves, contributing to further intercalation into the active material. This can be thought of as self-discharge of a local short-circuited battery comprising the plated Li and graphite surface. Delithiation shows simultaneous dissolution of the plated Li as well as slow de-intercalation from the active particle. Initially, most of the stripping occurs at the plated lithium, and the graphite surface in equilibrium with the plated Li stays at $c_s \sim 1$. Once all plated Li has been completely depleted from the system, the surface concentration immediately drops and a traversing delithiation front in the active material is observed, as expected.

Derivation of plating exchange current and degree of certainty: In our simulation, we find the plating exchange current based on projected area $i_{0,pl}$ to be 2.2 A/m^2 and the one based on microscopic surface area $i_{0,pl,m}$ to be 7×10^3 $\tilde{t}^{-1/2}$ A/m^2, where we report only one significant digit, due to uncertainty in active area and other parameters. Despite the seemingly crude approximations here, however, we believe this value is the most accurate to date, since we directly observe the active region of metal growth, while fitting to a model that captures the coupling to intercalation with validation from other experiments.

A browse through literature to compare our obtained exchange current value reveals there is little agreement on its order of magnitude: values of $i_{0,pl}$ ranging from 10^{-3} A/m^2 to 10^2 A/m^2

have been reported for lithium growth on carbon electrodes [17, 20–23]. To our knowledge, this is the first estimation of plating exchange current from direct in-situ optical data. The order of magnitude of the initial value of exchange current $i_{0,pl} \sim 2.2\ A/m^2$ agrees well with that reported by the direct measurements of Kushima et al. [17]. However, since visual estimation of growing lithium nuclei is challenging, since individual Li whiskers can be on the order of a few hundred nanometers [17], our theoretical prediction is primarily an order-of-magnitude estimate resulting from the growth of the first cluster of plated lithium nuclei.

The lithium-organic electrolyte interfacial energy γ is an important thermodynamic parameter describing the kinetic critical radius of lithium nuclei during the onset of plating. It also affects the degree of certainty in the prediction of the plating exchange current $i_{0,pl}$. In this work, we use reported by Lu et al. [24] which was derived out of direct experimental measurements of contact angles of various organic electrolytes on pure Li metal in an inert atmosphere at steady state. In their work, analysis of the contact angle data to determine surface tension γ was done using Young's equation and the Zisman approach [25–27]. Historically, due to absence of direct experimental measurements, theoretical results from Mullins-Sekerka type linear stability analyses were used to describe electrodeposition of metals in aqueous electrolytes [12, 28–30]. Aogaki and Makino (1979) [29], and Sundstrom and Bark (1995) [30] independently established the theory for interfacial stability for metal electrodeposition in aqueous systems using linear stability analysis. In 1998, Yamaki et al. [31] used the above theories to recommend a lower bound to the value of interfacial energy for lithium-organic electrolyte systems, approximately $0.2Nm^{-1}$, in absence of any experimental data at the time. Interestingly, these results have been widely used in lithium nucleation and growth modeling in organic electrolytes without any validation until as recently as 2017 [13, 32–34]. Upon comparison to the direct experimental results of Lu et al. [24], one can find that the interfacial energy recommendation by Yamaki et al. and predecessors and consequently that of contemporary lithium nucleation models are erroneous by about one order of magnitude. Admittedly, the contact angle measurements done by Lu et al. [24] are at steady-state and one could expect a deviation of the actual interfacial energy in unsteady state systems such as growing lithium nuclei on graphite. One way this could be directly validated is by observing in-situ critical nucleus size (using high resolution techniques such as in-situ atomic force microscopy or high-energy X-ray diffraction) and correlating the observed nucleation barrier V_n to the interfacial energy using Eq. S17. We will address this uncertainty and benchmark the theory against direct critical radius measurements using a porous electrode model in a future publication.

List of parameters:

Variable	Description	Value	Reference
$k_{0,int}$	Intercalation exchange current	1 A/m^2	[18]
$i_{0,pl}$	Plating reaction rate constant based on projected surface area	2 A/m^2	fitted
$i_{0,pl,m}$	Plating reaction rate constant based on microscopic surface area	7×10^3 $\tilde{t}^{-1/2}$ A/m^2	fitted, Eq. S19
N	Number of growing Li nuclei during plating	5.7×10^8	assumed
$V_{0,n}$	Nucleation potential for critical volume	0.15 V	experiments
A_{edge}	Edge-plane area for HOPG particle	0.1 mm^2	experiments
λ	Reorganization energy for graphite intercalation	$5k_BT$	[35, 36]
Ω	Molar volume of lithium	12.99 cm^3/mol	[13]
γ	Li-electrolyte interfacial energy	0.49 J/m^2	[24]

The equation for the homogeneous chemical potential μ_h is taken from Appendix A of Ref [4],

given below:

$$\mu_h = 0.18 + \mu_a + \mu_b + \mu_c + \mu_d + \mu_e$$

$$\mu_a = RT\left[\left(-40exp\left(-\frac{\tilde{c}}{0.015}\right) + 0.075\left(\tanh\left(\frac{\tilde{c}-0.17}{0.02}\right) - 1\right) + \tanh\left(\frac{\tilde{c}-0.22}{0.04} - 1\right)\right) S_D(\tilde{c}, 0.35, 0.05)\right]$$

$$\mu_b = -RT\frac{0.05}{\tilde{c}^{0.85}}$$

$$\mu_c = 10RTS_U(\tilde{c}, 1, 0.045)$$

$$\mu_d = 6.12RT(0.4 - \tilde{c}^{0.98})S_D(\tilde{c}, 0.49, 0.045)S_U(\tilde{c}, 0.35, 0.05)$$

$$\mu_e = RT(1.36(0.74 - \tilde{c}) + 1.26)S_U(\tilde{c}, 0.5, 0.02)$$

$$S_U(x, x_c, \delta) = 0.5\left(\tanh\left(\frac{x - x_c}{\delta}\right) + 1\right)$$

$$S_D(x, x_c, \delta) = 0.5\left(-\tanh\left(\frac{x - x_c}{\delta}\right) + 1\right)$$

[1] M. Z. Bazant, Accounts of Chemical Research **46**, 1144 (2013), arXiv:arXiv:1208.1587v5.

[2] M. Heß and P. Novák, Electrochimica Acta **106**, 149 (2013).

[3] S. J. Harris, A. Timmons, D. R. Baker, and C. Monroe, Chemical Physics Letters **485**, 265 (2010).

[4] K. E. Thomas-Alyea, C. Jung, R. B. Smith, and M. Z. Bazant, Journal of The Electrochemical Society **164**, E3063 (2017).

[5] K. G. Gallagher, S. E. Trask, C. Bauer, T. Woehrle, S. F. Lux, M. Tschech, P. Lamp, B. J. Polzin, S. Ha, B. Long, *et al.*, Journal of The Electrochemical Society **163**, A138 (2016).

[6] A. M. Colclasure, T. R. Tanim, A. N. Jansen, S. E. Trask, A. R. Dunlop, B. J. Polzin, I. Bloom, D. Robertson, L. Flores, M. Evans, *et al.*, Electrochimica Acta **337**, 135854 (2020).

[7] A. Pei, G. Zheng, F. Shi, Y. Li, and Y. Cui, Nano letters **17**, 1132 (2017).

[8] G. Wertheim, P. T. M. Van Attekum, and S. Basu, Solid State Communications **33**, 1127 (1980).

[9] J. W. Cahn and J. E. Hilliard, Journal of Chemical Physics **28**, 258 (1958).

[10] K. Persson, Y. Hinuma, Y. S. Meng, A. Van der Ven, and G. Ceder, Physical Review B **82**, 125416 (2010).

[11] D. A. Cogswell and M. Z. Bazant, Nano Letters **13**, 3036 (2013), 1304.0105.

[12] E. Khoo, H. Zhao, and M. Z. Bazant, Journal of The Electrochemical Society **166**, A2280 (2019).

[13] D. R. Ely and R. E. García, Journal of the Electrochemical Society **160**, A662 (2013).

[14] A. N. Kolmogorov, *On the Statistical Theory of Crystallization of Metals [in Russian]* (Izv. Akad. Nauk SSSR, Ser. Mat. No. 3, 1937).

[15] M. Avrami, J. Chem. Phys **8**, 212 (1940).

[16] J. William and R. Mehl, Trans. Metall. Soc. AIME **135**, 416 (1939).

[17] A. Kushima, K. P. So, C. Su, P. Bai, N. Kuriyama, T. Maebashi, Y. Fujiwara, M. Z. Bazant, and J. Li, Nano Energy **32**, 271 (2017).

[18] R. B. Smith, E. Khoo, and M. Z. Bazant, The Journal of Physical Chemistry C **121**, 12505 (2017).

[19] Y. Zeng and M. Z. Bazant, SIAM Journal on Applied Mathematics **74**, 980 (2014).

[20] H. Ge, T. Aoki, N. Ikeda, S. Suga, T. Isobe, Z. Li, Y. Tabuchi, and J. Zhang, Journal of The Electrochemical Society **164**, A1050 (2017).

[21] P. Arora, M. Doyle, and R. E. White, Journal of The Electrochemical Society **146**, 3543 (1999).

[22] X.-G. Yang, Y. Leng, G. Zhang, S. Ge, and C.-Y. Wang, Journal of Power Sources **360**, 28 (2017).

[23] C. von Lüders, J. Keil, M. Webersberger, and A. Jossen, Journal of Power Sources **414**, 41 (2019).

[24] Y. Lu, Z. Tu, and L. A. Archer, Nature materials **13**, 961 (2014).

[25] W. A. Zisman, Industrial & Engineering Chemistry **55**, 18 (1963).

[26] M. Gindl, G. Sinn, W. Gindl, A. Reiterer, and S. Tschegg, Colloids and Surfaces A: Physicochemical and Engineering Aspects **181**, 279 (2001).

[27] M. Dahbi, D. Violleau, F. Ghamouss, J. Jacquemin, F. Tran-Van, D. Lemordant, and M. Anouti, Industrial & engineering chemistry research **51**, 5240 (2012).

[28] C. P. Nielsen and H. Bruus, Physical Review E **92**, 052310 (2015).

[29] R. Aogaki and T. Makino, Electrochimica Acta **26**, 1509 (1981).

[30] L.-G. Sundström and F. H. Bark, Electrochimica acta **40**, 599 (1995).

[31] J.-i. Yamaki, S.-i. Tobishima, K. Hayashi, K. Saito, Y. Nemoto, and M. Arakawa, Journal of Power Sources **74**, 219 (1998).

[32] R. Akolkar, Journal of Power Sources **232**, 23 (2013).

[33] D. Wang, W. Zhang, W. Zheng, X. Cui, T. Rojo, and Q. Zhang, Advanced Science **4**, 1600168 (2017).

[34] C. Monroe and J. Newman, Journal of The Electrochemical Society **150**, A1377 (2003).

[35] D. Fraggedakis, M. McEldrew, R. B. Smith, Y. Krishnan, Y. Zhang, W. Chueh, P. Bai, Y. Shao-Horn, and M. Z. Bazant, "Theory of coupled ion-electron transfer kinetics," (2020).

[36] D. Fraggedakis, Y. Zhang, T. Gao, R. M. Stephens, Y. Shao-Horn, and M. Z. Bazant, (2020).

SUPPLEMENTARY FIGURES

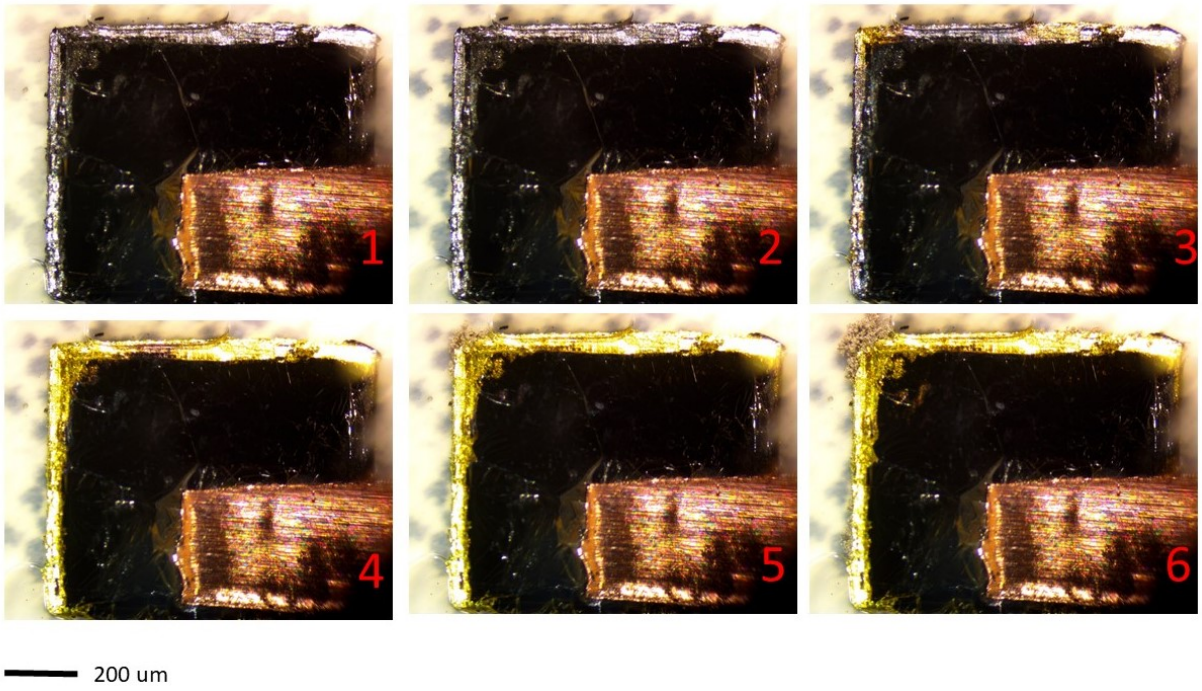

FIG. S1. The images of HOPG particle A during lithiation.

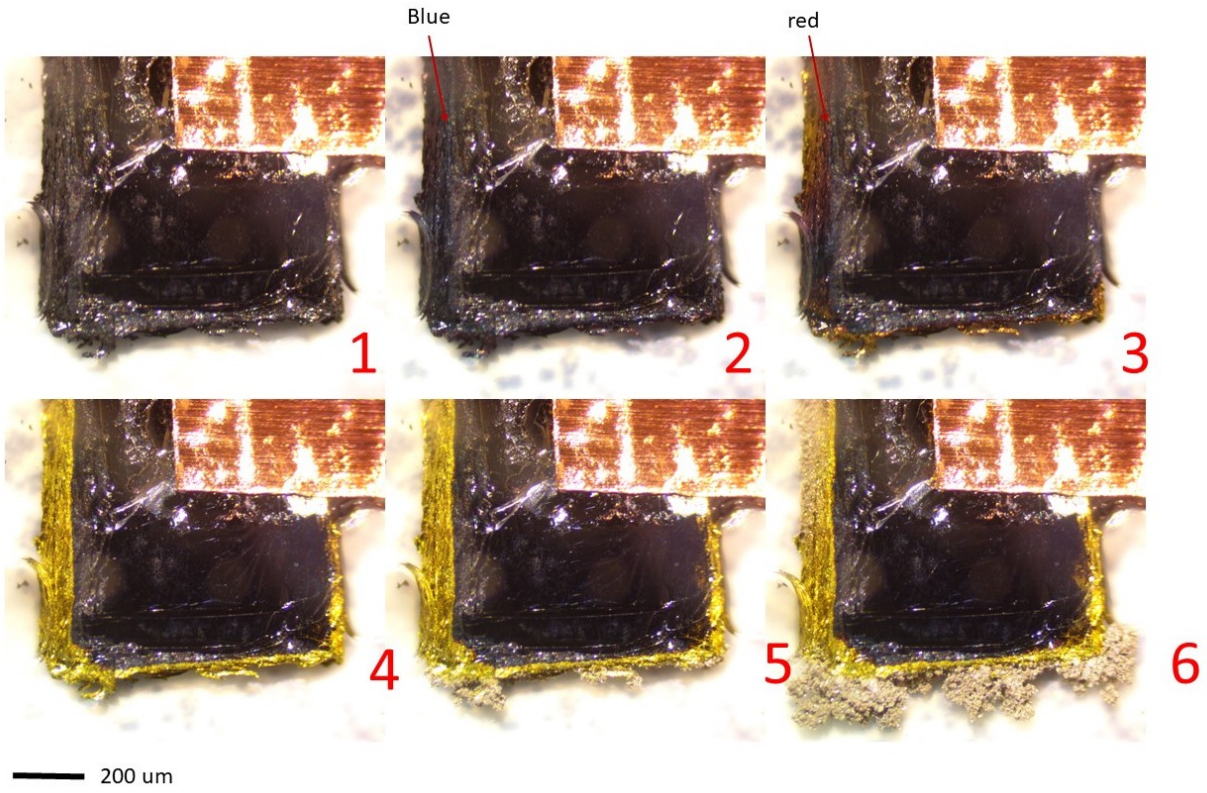

FIG. S2. The images of HOPG particle C during lithiation.

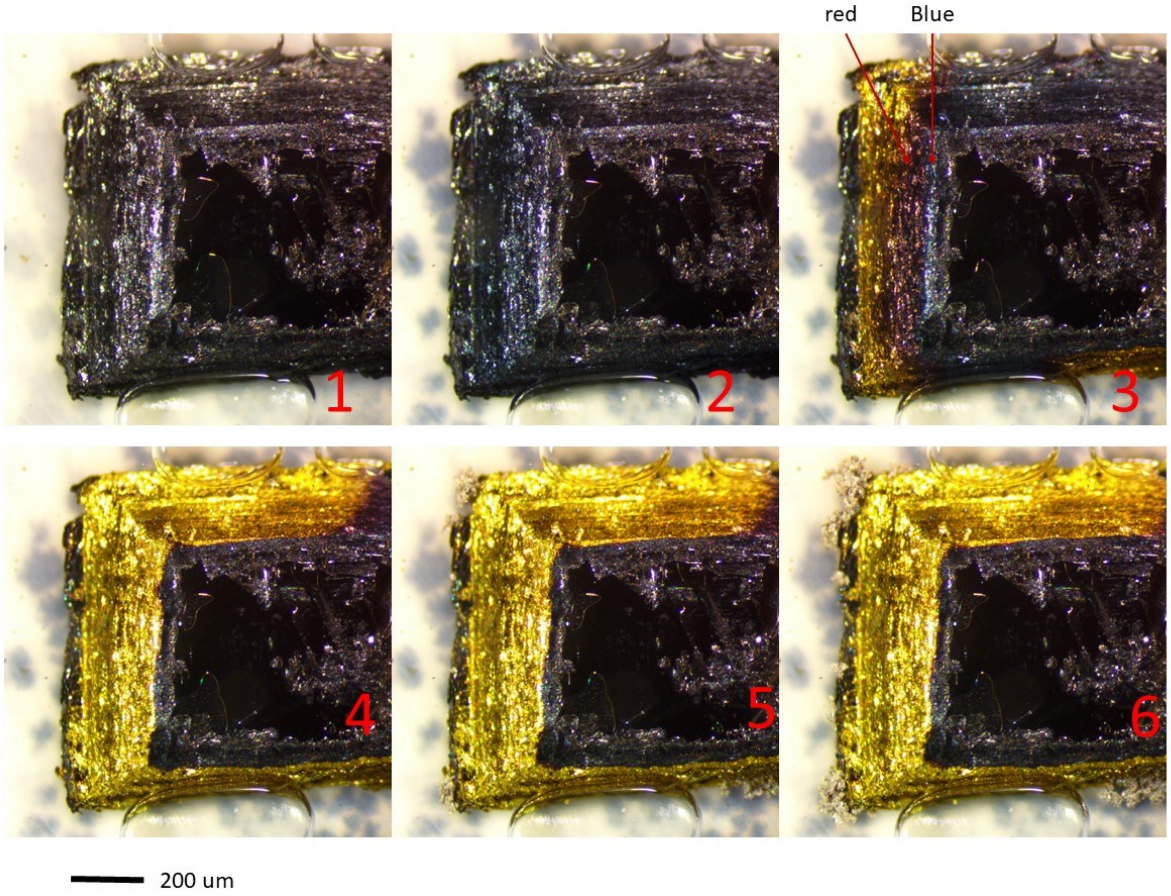

FIG. S3. The images of HOPG particle D during lithiation.

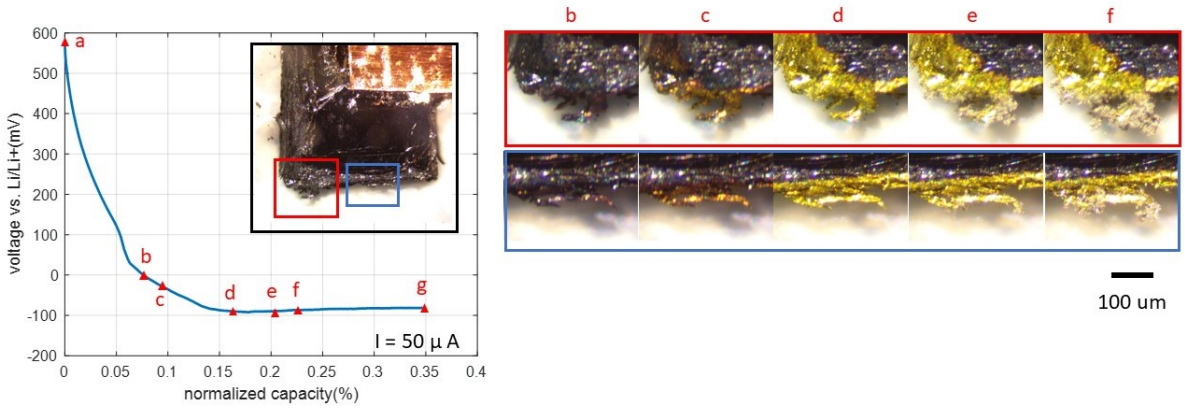

FIG. S4. The voltage and zoom-in images of particle C during lithiation.

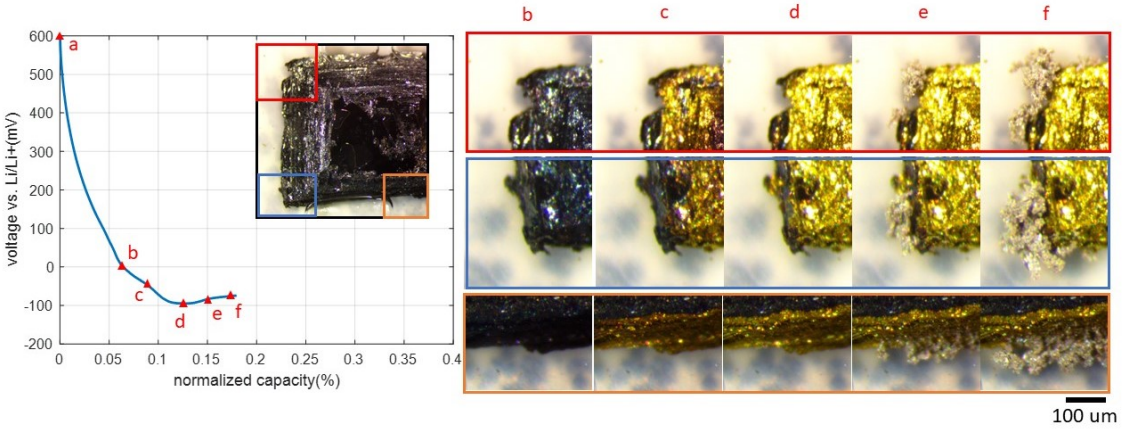

FIG. S5. The voltage and zoom-in images of particle D during lithiation.

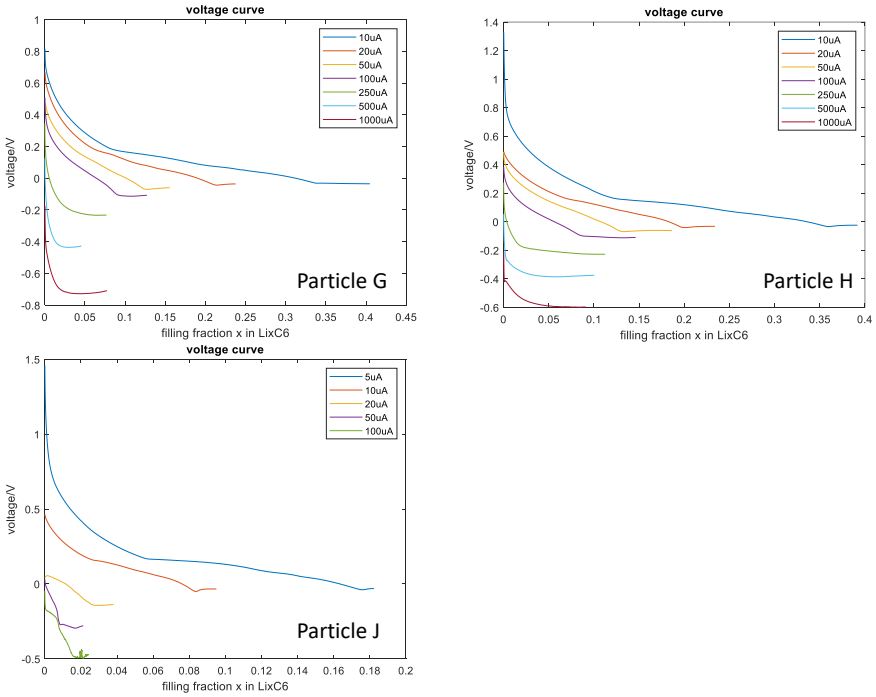

FIG. S6. Voltage curves of three different particles at different currents

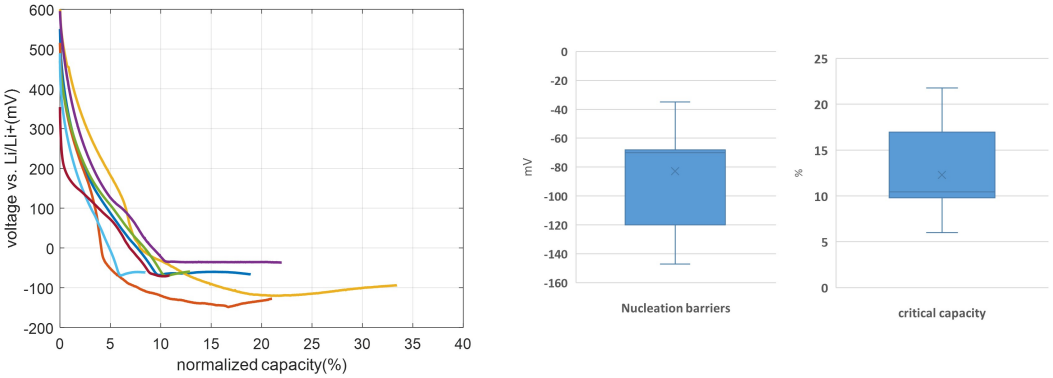

FIG. S7. voltage curves of seven different particles at 50 μA, and box plots of the nucleation barrier and critical capacity for nucleation obtained from the voltage curves

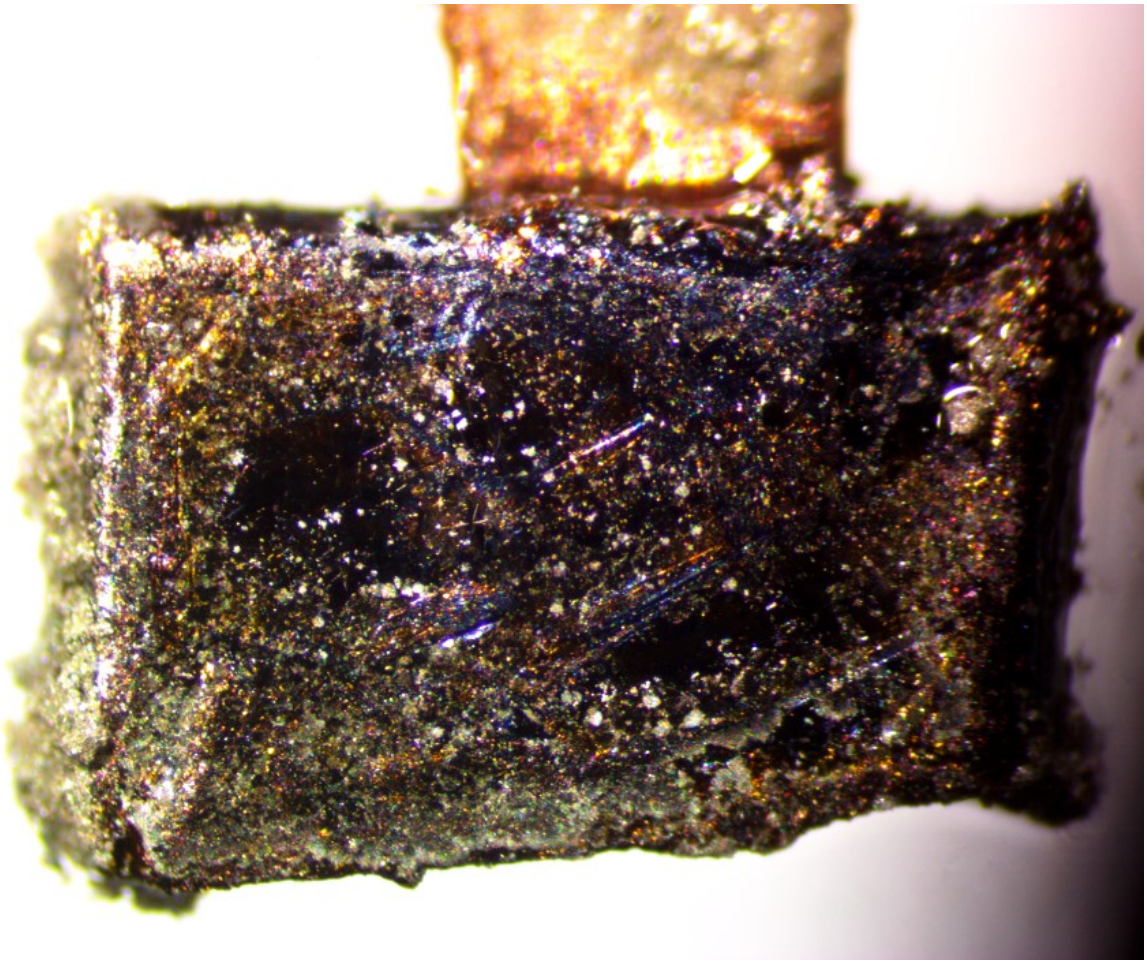

FIG. S8. Optical image of the bottom side of one HOPG particle after 18 % charge

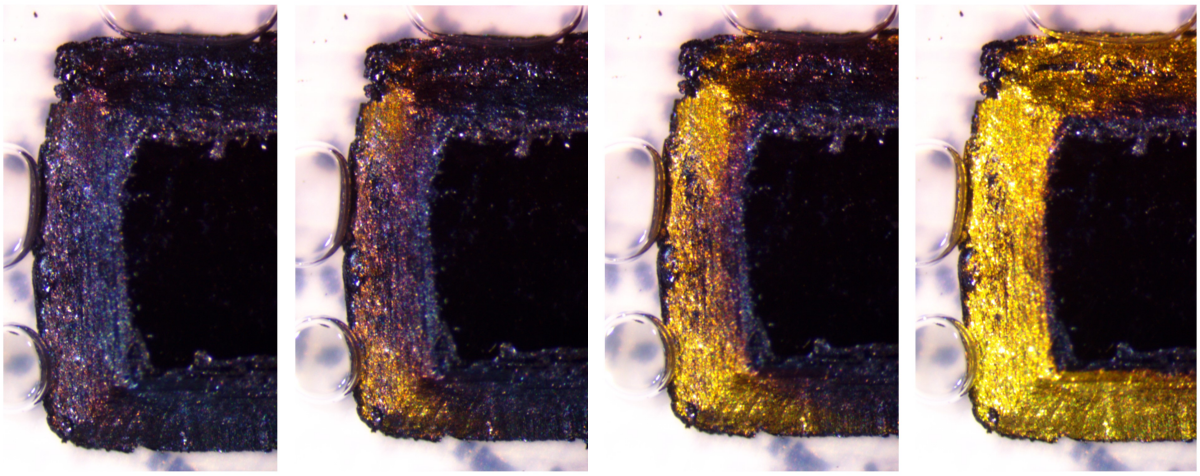

FIG. S9. A particle with trapezoid a-c cross section at 50 μA.The lithiation of graphite starts at the bottom of the particle, and then propagates upward toward the top surface that is facing the camera.

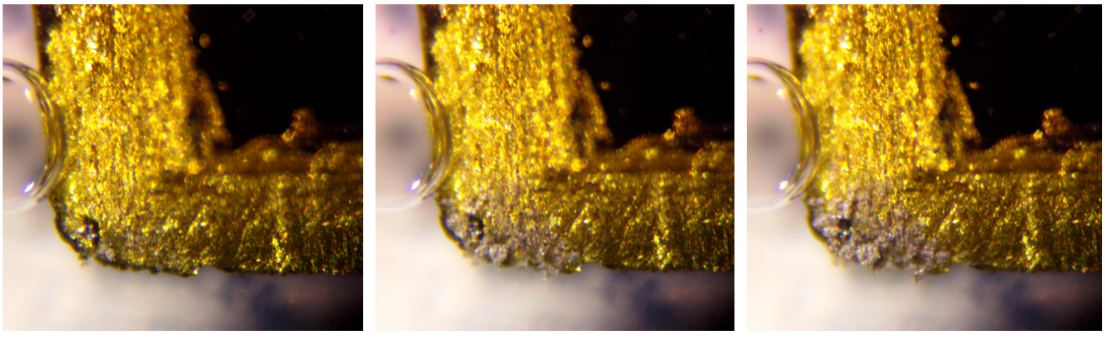

FIG. S10. Zoom-in of the above particle. The onset condition of Li plating is the same with particles A and B, i.e. Li plating only starts when the edge surface is saturated (all edge surface becomes gold).

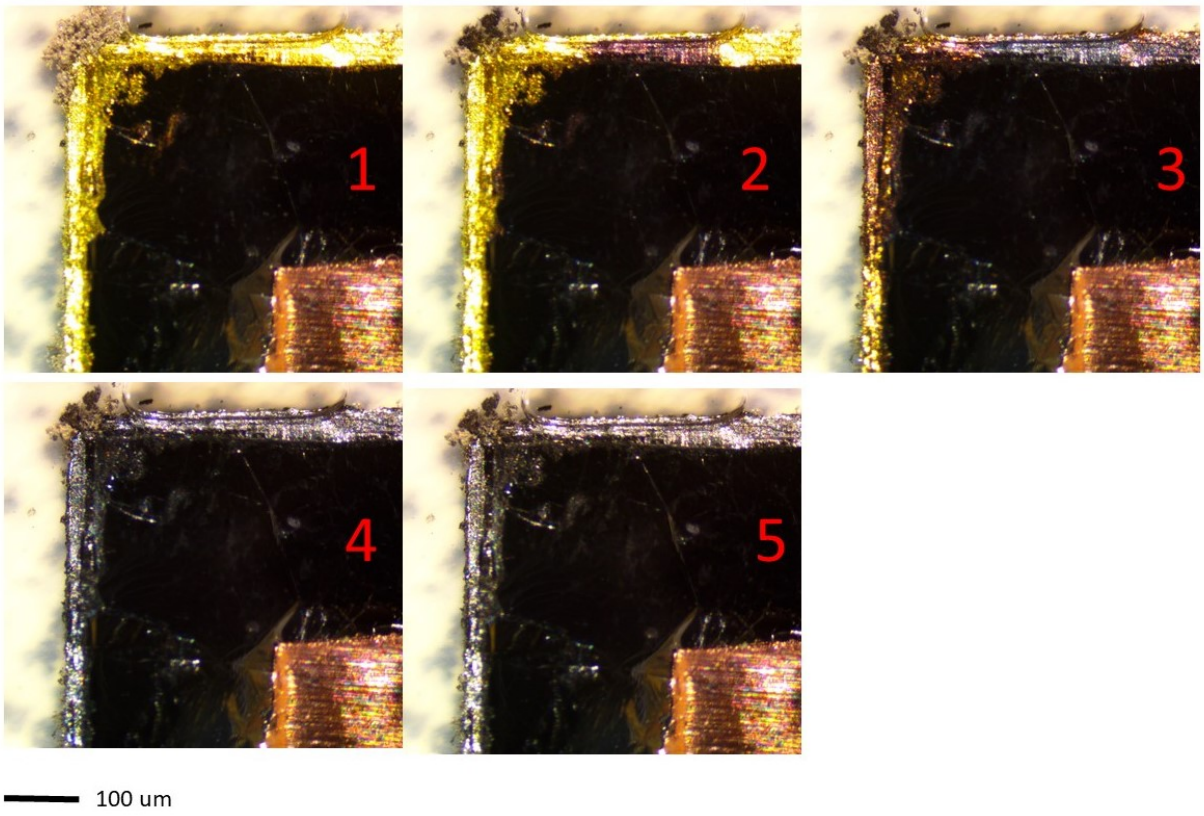

FIG. S11. The rest of HOPG particle A

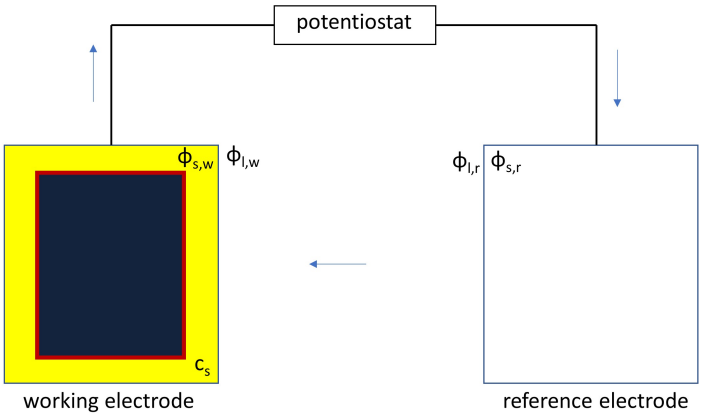

FIG. S12. **The schematic for reactions at working and reference electrode**

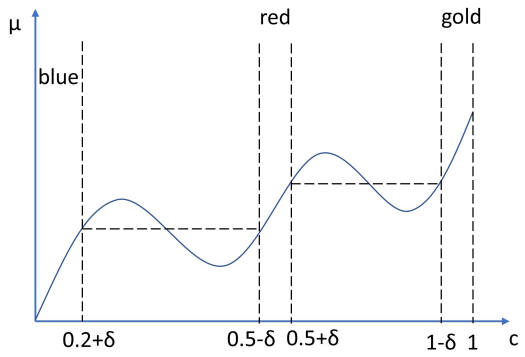

FIG. S13. **Diffusional chemical potential as a function of local concentration**

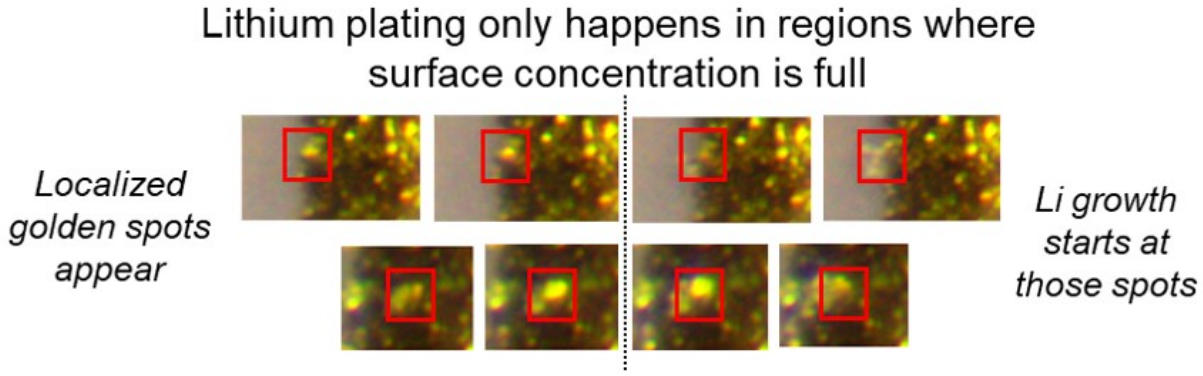

FIG. S14. **Snapshots of points on electrode, that turn from bright gold to silver, demonstrating that mossy lithium nucleates and grows only from regions where particles are full**

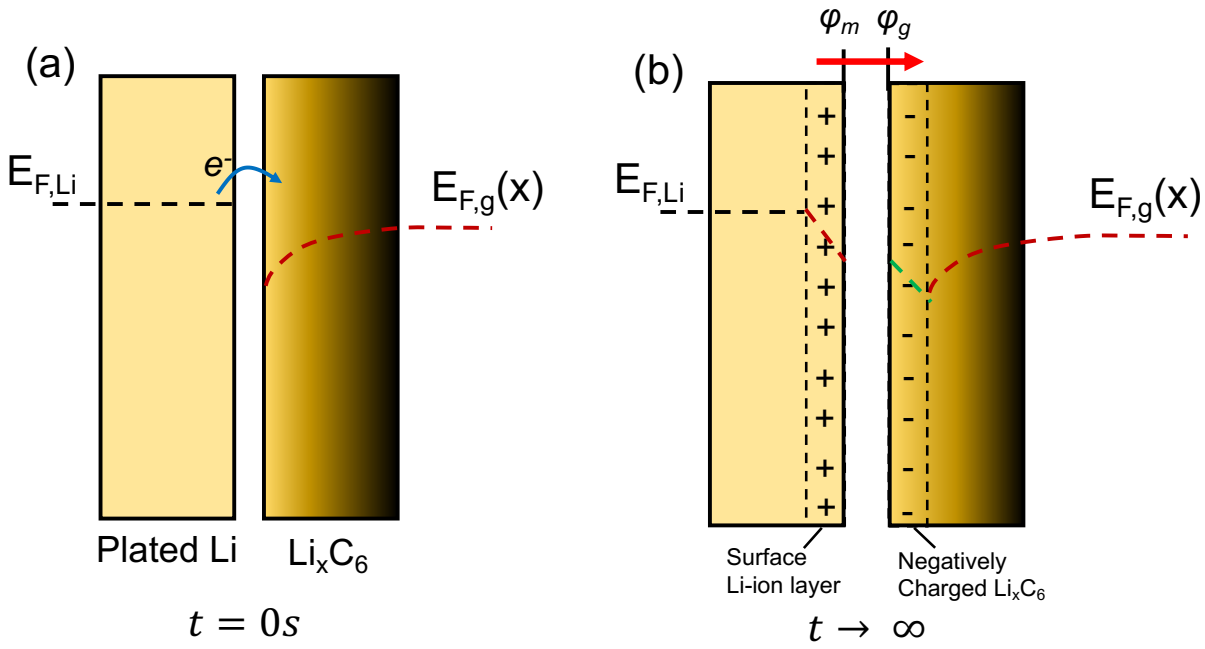

FIG. S15. **The schematic for the formation of contact potentials**

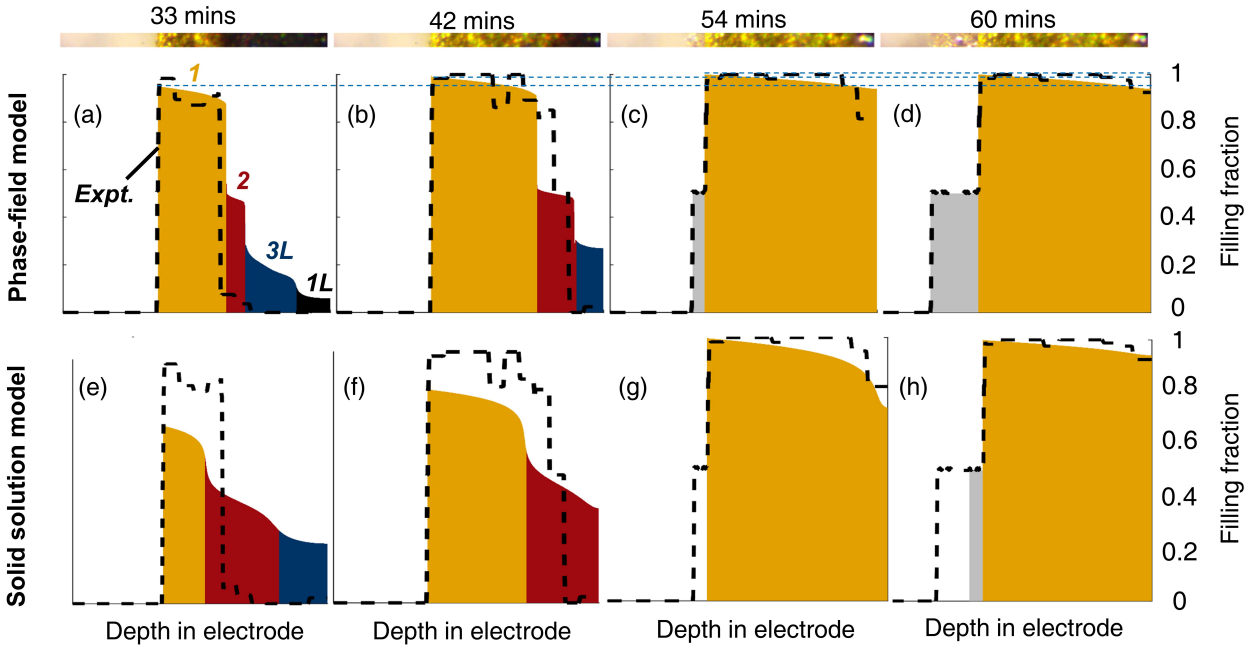

FIG. S16. Model predictions of Li concentration profiles compared with experimental data during lithiation, under a driving current I = 5 mA/cm^2. (a-d) Cahn-Hilliard Reaction model (e-h) Solid solution model

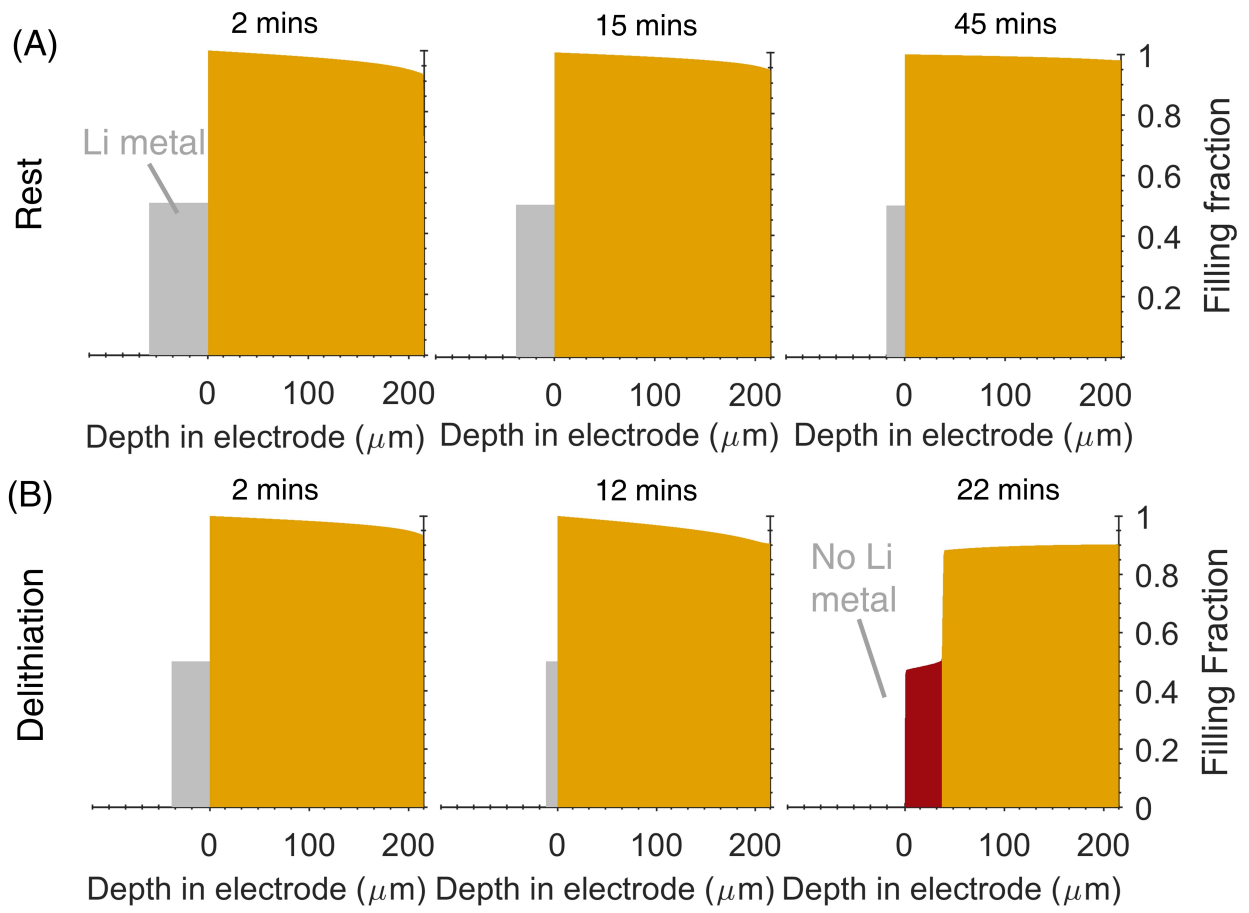

FIG. S17. Model predictions of Li concentration profiles (A) during 45 min rest and (B) under delithiation with a driving current I = 5 mA/cm^2